Fatigue-constrained topology optimization using the constrained natural element method

Yanda Chen, Eric Monteiro, Imade Koutiri, Véronique Favier

Fatigue-constrained Topology Optimization Using the Constrained Natural Element Method

Yanda Chen[a], Eric Monteiro[a], Imade Koutiri[a], Véronique Favier[a]

[a]*Laboratory PIMM, Arts et Metiers Institute of Technology, CNRS, CNAM, HESAM Universite, 151 Bd de l'Hôpital, Paris, 75013, France*

Abstract

This research presents a topology optimization framework to achieve volume minimization with multi-axial high cycle fatigue criteria constraints by constrained natural element method. To solve the local minimization problem, the method based on the augmented Lagrangian formula is adopted. Special attention is given to the optimization results based on the stress-invariant fatigue criteria and the critical plane fatigue criteria under different loading conditions, including proportional and non-proportional loading.

Keywords: Topology optimization, High cycle fatigue, Constrained natural element method, Augmented Lagrangian formula

1. Introduction

Topology optimization is a sophisticated structural design methodology that generates novel and efficient configurations. The optimized structures are lightweight, but challenging to create through traditional ways. However, topology optimization designs are well suited for additive manufacturing processes that have more relaxed design rules and can easily replicate complex shapes without additional cost. In the modern industry, the combination of topology optimization and additive manufacturing has a wide range of applications to maximize the advantages and potential of both techniques (Liu et al. (2018); Ibhadode et al. (2023)).

Additive manufactured materials and components for critical load-bearing applications are usually subjected to cyclic loading during their service life.

Email address: yanda.chen@ensam.eu (Yanda Chen)

These loads can be out of phase and in different frequencies which will produce complex bi-axial or tri-axial stress states (Nalli et al. (2021)). Structural fatigue under complex stress state can lead to sudden and catastrophic failure due to its progressive and insidious nature. Therefore, it is very important to take the multi-axial fatigue factors into account and reasonably predict the fatigue life of the structure in the design stage.

A series of multi-axial fatigue criteria have been developed and improved during the past decades. However, the applicability of those criteria are related to load and material characteristics. Wang and Yao (2004) found that the prediction of most fatigue criteria had little deviation from the experimental results under proportional loading, however, the errors were larger under non-proportional loading, and the degree of which varies with materials. Similar conclusions were also reached by Papadopoulos et al. (1997) and Matsubara et al. (2018). Therefore, the selection of HCF criteria should be prudent when faced with complex loading conditions. Otherwise, the prediction results are quite different from one criterion to another (Dantas et al. (2021)). For each topology optimization problem subjected to fatigue constraints, it is difficult to determine which class of fatigue criteria produce better predictions. In this study, the most interesting aspect is the comparison of the topology optimization results under different multi-axial fatigue criteria constraints for different benchmark problems and loading conditions.

Several static and quasi-static fatigue models have been developed for topology optimization of linear elastic structures to simplify the computational cost under a large number of load cycles. Holmberg et al. (2014) imposed stress constraints instead of fatigue constraints in topology optimization. Oest and Lund (2017) adopted the rainflow counting method to handle proportional load histories. Jeong et al. (2018) developed a topology optimization model based on equivalent static load method considering variable amplitude load. Zhang et al. (2018) predicted the fatigue life of non-proportional loads by using signed von Mises stresses. Suresh et al. (2020) proposed a fatigue-constrained topology optimization formulation based on continuous-time approach to consider general load histories including non-proportional loads. Chen et al. (2020) considered cumulative fatigue damage in topology optimization and discussed the effects of damage penalty parameters and load parameters on the final design. Slebioda et al. (2023) proposed a topology optimization method with infinite fatigue life constraint under non-proportional loading based on signed von Mises stress. In the aforementioned literature, the fatigue-constrained topology optimization studies

use finite element method to solve the partial differential equations and employ aggregation techniques to approximate the maximum value of the constraints. However, the widely used Lagrangian-type finite elements suffer from mesh dependence (Sigmund and Petersson (1998); Talischi et al. (2009)), and the aggregation technique loses control over the local behavior (París et al. (2009); Verbart et al. (2016); Senhora et al. (2020)). Recently, Chen et al. (2023) presented a topology optimization framework to achieve volume minimization with stress constraints by constrained natural element method (CNEM) and the local optimal solution is obtained through the augmented Lagrangian formula. Compared to previous studies, CNEM is less affected by the discretization scheme and the augmented Lagrangian approach reduces the cost associated with a large number of constraints while providing a more consistent model than aggregation techniques.

This study aims to investigate the performance of CNEM in solving topology optimization problems with multi-axial high cycle fatigue (HCF) criteria constraints. Particular attention is paid to the fatigue criteria based on the critical plane, a class of problems that has not been widely implemented in topology optimization so far. The reminder of this paper is organized as follows. Section 2 introduces several common multi-axial HCF criteria. Section 3 presents the topology optimization problem with fatigue constraints for continuum structures, and several numerical examples are shown in Section 4, followed by a discussion of the predicted results of the fatigue criterion under different loading conditions in Section 5. Finally, Section 6 gives concluding remarks to complete the paper. The procedure of sensitivity analysis is given in Appendix A.

2. Multi-axial high cycle fatigue criteria

Multi-axial fatigue is a common problem for many engineering structures and components. Accurate fatigue life prediction is necessary to guarantee the long-term integrity of these structures and components. A wide range of multi-axial fatigue models have been proposed to predict fatigue life and they can be categorized into four groups: stress-based, strain-based, energy-based and fracture mechanics-based (Wei and Liu (2020)). The HCF is caused by small strain (mainly elastic) under a large number of load cycles ($\geq 10^5$ cycles), as shown in Fig. 1. Therefore, the most commonly used criteria for this kind of fatigue problem is the stress-based criteria.

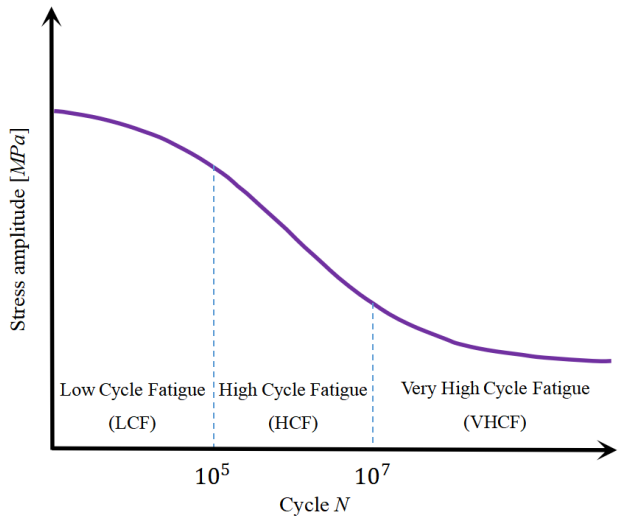

Figure 1: General representation of the S-N diagram

In this study, HCF life is modeled and the inertial effects are neglected, so that the stress state at each moment in the loading history is obtained by linear elastic analysis. In principle, the stress-based criteria can be classified into the following groups: criteria based on stress invariant, such as Sines (Sines (1959)) and Crossland (Crossland (1956)) criteria, critical plane models proposed by Matake (Matake (1977)), Findley (Findley (1959)) and Dang Van (Dang Van et al. (1989)), criteria based on the average stress, i.e., the integral approaches proposed by Papadopoulos (Papadopoulos (2001)) and Liu and Zenner (Liu and Zenner (2003)), the model based on moving durable surface in stress space (Ottosen et al. (2008); Brighenti et al. (2012)). For a comprehensive compilation of different HCF models, please refer to Socie and Marquis (Socie and Marquis (1999)). Due to the calculation cost, the average stress method is not considered in this study. The predicted fatigue damage based on moving durable surface model corresponds well to experimental results under cyclic proportional stress. However, it has limitations in correctly predicting damage evolution in rotary stress states (Lindström et al. (2020)), thus, nor is it considered here. Several representative criteria from the first two categories are presented in Table 1, where $\sqrt{J_{2,a}}$ is the amplitude of the second stress invariant, $\sigma_{H,mean}$ and $\sigma_{H,max}$ represent the mean and maximum hydrostatic stress respectively, τ_a is the amplitude of shear stress and $\sigma_{n,\max}$ is the maximum value of normal stress.

Table 1: Several HCF criteria based on stress

HCF criteria	Model formula	Parameter
Stress invariant	Sines (Sines (1959))	$\alpha_s = \frac{6t_{-1}}{f_0} - \sqrt{3}$
	$g = \sqrt{J_{2,a}} + \alpha_s \sigma_{H,mean} \leq \beta_s$	$\beta_s = t_{-1}$
	Crossland (Crossland (1956))	$\alpha_c = \frac{3t_{-1}}{f_{-1}} - \sqrt{3}$
	$g = \sqrt{J_{2,a}} + \alpha_c \sigma_{H,max} \leq \beta_c$	$\beta_c = t_{-1}$
Critical plane	Findley (Findley (1959))	$\alpha_f = \frac{2 - \frac{f_{-1}}{t_{-1}}}{2\sqrt{\frac{f_{-1}}{t_{-1}} - 1}}$
	$g = \max_{\theta} (\tau_a + \alpha_f \sigma_{n,\max}) \leq \beta_f$	$\beta_f = \frac{f_{-1}}{2\sqrt{\frac{f_{-1}}{t_{-1}} - 1}}$
	Matake (Matake (1977))	$\alpha_m = \frac{2t_{-1}}{f_{-1}} - 1$
	$g = \max_{\theta} (\tau_a) + \alpha_m \sigma_{n,\max} \leq \beta_m$	$\beta_m = t_{-1}$
	Dang Van (Dang Van et al. (1989))	$\alpha_{dv} = \frac{3t_{-1}}{f_{-1}} - \frac{3}{2}$
	$g = \max_{\theta} (\tau_a) + \alpha_{dv} \sigma_{H,\max} \leq \beta_{dv}$	$\beta_{dv} = t_{-1}$

All of the HCF criteria in Table 1 consist of two stress components associated with the material parameters which are related to the weight of the damage effect. The parameters α and β can be identified by uni-axial fatigue tests, where t_{-1} is the fully reversed torsional fatigue limit, f_0 and f_{-1} represent the fully repeated and fully reversed bending fatigue limit respectively. The stress terms $J_{2,a}$ and σ_H during the load cycle $0 \leq t \leq T$ can be calculated as follows:

$$\begin{cases} J_{2,a} = (\boldsymbol{\sigma}_a)^T \boldsymbol{M} \boldsymbol{\sigma}_a \\ \sigma_{H,mean} = \frac{(\sigma_{xx,mean} + \sigma_{yy,mean})}{3} \\ \sigma_{H,max} = \max\limits_t \left[\frac{\sigma_{xx}(t) + \sigma_{yy}(t)}{3} \right] \end{cases} \tag{1}$$

where the subscripts a and $mean$ represent the amplitude and mean values of Cauchy stress vector at any position $\boldsymbol{x}$:

$$\begin{cases} \boldsymbol{\sigma}_a = \left\{ \max\limits_t [\boldsymbol{\sigma}(t)] - \min\limits_t [\boldsymbol{\sigma}(t)] \right\} /2 \\ \boldsymbol{\sigma}_{mean} = \left\{ \max\limits_t [\boldsymbol{\sigma}(t)] + \min\limits_t [\boldsymbol{\sigma}(t)] \right\} /2 \end{cases} \tag{2}$$

and

$$\boldsymbol{M} = \begin{bmatrix} 1/3 & -1/6 & 0 \\ -1/6 & 1/3 & 0 \\ 0 & 0 & 1 \end{bmatrix} \tag{3}$$

for 2D plane stress state.

The implementation of the first type of criteria based on stress invariants in the calculations is very straightforward, the difference between Sines and Crossland criteria is the use of the maximum or the mean value of the hydrostatic stress. An important feature of these criteria is that the stress parameters are independent of the specific plane orientation which leads to the simplicity of the solution. However, they are unable to specify the direction of potential fatigue cracks. Hence, their applicability is limited to the case where the principal axis of the alternating stress is fixed on the object. The most widely used approach is based on the concept of critical plane, where the stress state at the maximum loaded plane is assumed to be the cause of crack initiation. The identification of such a plane mainly consists of measuring the maximum damage plane or the plane with the maximum shear stress range. The fatigue criteria based on critical plane follows the same process. Firstly, the critical plane needs to be found by definition, and

second, whether the criteria is satisfied on this plane is checked. Note that the Matake and Dang Van criteria define only the plane with the maximum shear stress amplitude as the critical plane and denies any additional influence of other stress components. The characterization of the critical plane only as the plane of maximum shear stress amplitude may lead to ill-posed problems, since many different planes can experience the same value, therefore, it may be resonable to consider a second factor to determine the critical plane, as proposed in the Findley criterion. By introducing the above fatigue criteria into topology optimization, it is also possible to compare the effects of hydrostatic stress (average of the normal stresses) and normal stress on topology optimization results.

In order to better understand each criterion and to identify the trend of different criteria dealing with different loading conditions, Fig. 2 demonstrates the ability of the criteria to predict the fatigue behavior of additive manufactured Ti-6Al-4V alloy under uni-axial tension, combined tension-torsion and bi-axial tension loading. The latter two loading conditions are in-phase and have a stress ratio of -1. Due to missing fully repeated bending fatigue limit data f_0, the prediction of Sines under uni-axial tension loading is not plotted. The bi-axial ratio under bi-axial tension loading is given by $b_k = \sigma_{yy}(t)/\sigma_{xx}(t)$, and the case of $b_k = 1$ corresponds to equal bi-axial tension.

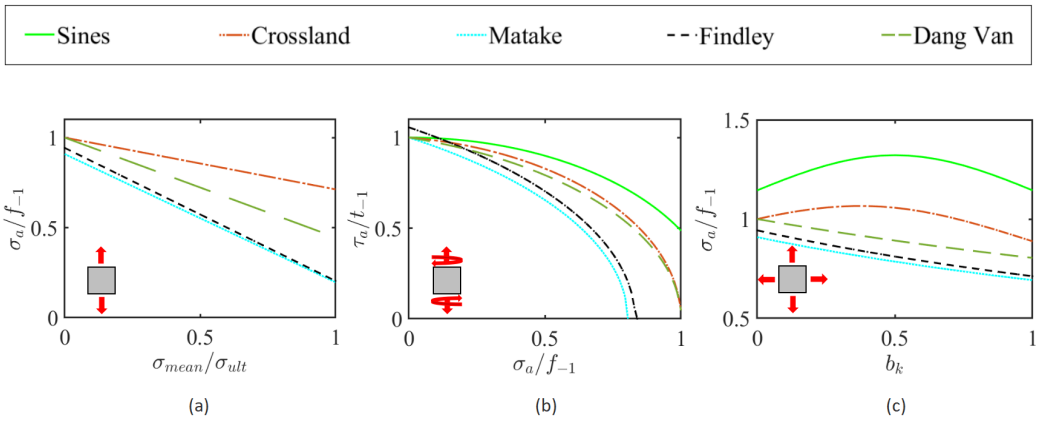

Figure 2: Prediction of HCF criteria with (a)uni-axial tension, (b) combined tension-torsion and (c) bi-axial tension loading

Although the effect of mean stress on fatigue life is not the goal of this study, all fatigue criteria predict a linear decrease in fatigue strength with

increasing mean stress under uni-axial tension loading, see Fig. 2(a). In the absence of mean stress, Crossland and Dang Van have the same predictions under uni-axial tension loading, while Dang Van shows a significantly faster decrease than Crossland as the mean stress increases. The other two critical plane based fatigue criteria, Matake and Findley, start slightly lower than the fully reversed bending fatigue limit under uni-axial tension loading, their slopes of decrease with increasing mean stress are slightly larger than Dang Van criterion. Under pure torsion loading, all criteria except Findley show the same prediction, as shown in Fig. 2(b). Since the parameter β for the Findley criterion is not equal to the fully reversed torsional fatigue limit, this leads to a slight deviation. However, all criteria give completely different predictions when tension and torsion are applied simultaneously. The HCF criteria considered in this study predict the nonlinear effect of bi-axial ratio under bi-axial tension loading, see Fig. 2(c). For the first kind of criterion based on the stress invariants, the fatigue strength increases at low bi-axial ratio, and then decreases. For the bi-axial ratios of $b_k = 0.5$ and $b_k = 0.4$, the beneficial effects of Sines and Crossland reach the maximum respectively. However, for the criterion based on critical plane, fatigue strength decreases with the increment of bi-axial ratio. In general, the fatigue criteria based on critical plane show more conservative predictions than the fatigue criteria based on stress invariant under simple cases.

The constant amplitude fatigue load can be divided into two types: proportional loading and non-proportional loading, as shown in Fig. 3. The proportional loading is presented by a $\psi = 0°$ phase difference, meaning that the stress at any point of the structure at any time can be represented by a time-dependent scalar multiplied by the stress at a specified reference time point for linear elastic problems, while a non-zero phase difference implies non-proportionality, in which case there is no such a scalar function. Therefore, when dealing with non-proportional loads, the superposition principle or the so called linear combination model adopted by Zhang et al. (2018) is used, that is, the stress state of any position $\boldsymbol{x}$ at any time t over any plane θ can be expressed as a linear combination of the stresses generated by the unit loads:

$$\boldsymbol{\sigma}(\boldsymbol{x}, t, \theta) = \sum_{l=1}^{n_f} \boldsymbol{c}_l \boldsymbol{\sigma}_{l,ref}(\boldsymbol{x}, \theta) \tag{4}$$

where n_f is the number of loads, $\boldsymbol{\sigma}_{l,ref}$ represents the stress vector corre-

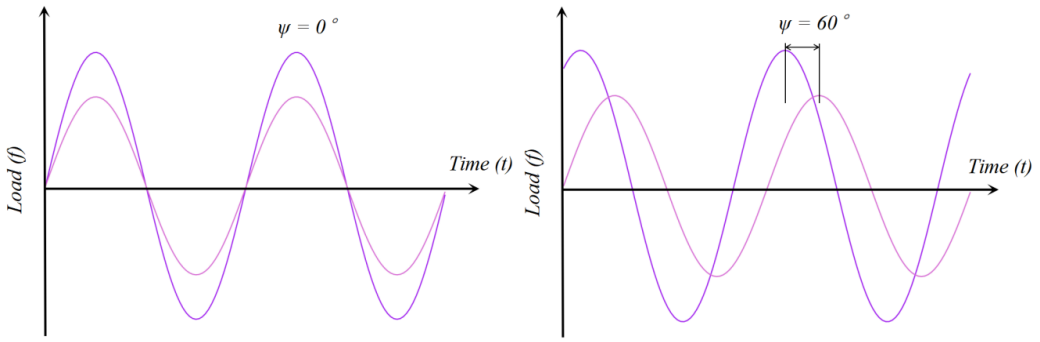

Figure 3: Proportional loading (left) and non-proportional loading (right)

sponding to l-th unit load over the specified plane, $\boldsymbol{c}_l$ is the stress ratio vector between l-th load and l-th unit load at time t over the plane, θ can be removed when the stress invariant method is adopted. Subsequently, the extreme values and amplitudes of the stresses over any plane are given by:

$$\begin{cases} \boldsymbol{\sigma}_{max}(\boldsymbol{x},\theta) = \sum_{l=1}^{n_f} \boldsymbol{c}_{l,max}\, \boldsymbol{\sigma}_{l,ref}(\boldsymbol{x},\theta) \\ \boldsymbol{\sigma}_{min}(\boldsymbol{x},\theta) = \sum_{l=1}^{n_f} \boldsymbol{c}_{l,min}\, \boldsymbol{\sigma}_{l,ref}(\boldsymbol{x},\theta) \\ \boldsymbol{\sigma}_{a}(\boldsymbol{x},\theta) = \frac{1}{2}\sum_{l=1}^{n_f} (\boldsymbol{c}_{l,max} - \boldsymbol{c}_{l,min})\, \boldsymbol{\sigma}_{l,ref}(\boldsymbol{x},\theta) \end{cases} \tag{5}$$

where $\boldsymbol{c}_{l,max}$ and $\boldsymbol{c}_{l,min}$ represent the coefficient vectors of stress extremes. When the load is proportional, n_f in Eqs.4 and 5 is always equal to 1 and $\boldsymbol{\sigma}_{ref}$ is the reference stress vector corresponding to any loading moment.

The critical plane method assumes that the fatigue life can be calculated from the damage in the critical plane at the critical point, and the damage located on all other planes does not affect the initiation of microcracks. The main computational challenge of this approach is to calculate the cumulative damage of many candidate planes at each point to discover the direction of the critical plane where the damage is maximized. However, this search can be simplified in the two-dimensional state where the critical plane is always constant.

At each point under study, a general plane Δ can be defined by its unit

normal vector $\boldsymbol{n}$, which can be described by the angle θ in 2D state, see Fig. 4, where θ is the inclination between $\boldsymbol{n}$ and the x-axis. Since the negative normal vector describes the same plane, the search space is further reduced to a semicircle. A simple procedure for discretizing this semicircle is to scan from 0° to 180° using predetermined angular increments. For example, when an increment of 1° is adopted, the stresses located in 180 planes need to be evaluated at each point for all load steps.

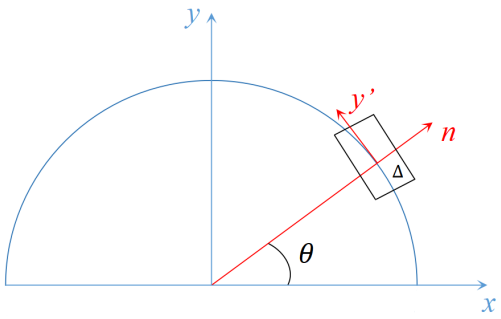

Figure 4: Determination of critical plane in 2D

The stress vector $\boldsymbol{S}(t,\theta)$ acting on such a plane can be decomposed into the normal stress component $\sigma_n(t,\theta)$ and the in-plane shear stress vector $\boldsymbol{\tau}(t,\theta)$. Given the plane Δ, the magnitude of $\sigma_n(t,\theta)$ changes during the load cycles, but the direction is always consistent with the normal vector $\boldsymbol{n}$ of Δ. Therefore, $\sigma_n(t,\theta)$ can be completely described by its algebraic value:

$$\sigma_n(t,\theta) = \boldsymbol{S}(t,\theta)\cdot\boldsymbol{n} = \boldsymbol{n}\cdot\boldsymbol{\sigma}(t,\theta)\cdot\boldsymbol{n} \tag{6}$$

The orthogonal projection of $\boldsymbol{S}(t,\theta)$ on Δ gives the in-plane shear stress $\boldsymbol{\tau}(t,\theta)$:

$$\boldsymbol{\tau}(t,\theta) = \boldsymbol{S}(t,\theta) - \sigma_n(t,\theta)\boldsymbol{n} = \boldsymbol{\sigma}(t,\theta)\cdot\boldsymbol{n} - [\boldsymbol{n}\cdot\boldsymbol{\sigma}(t,\theta)\cdot\boldsymbol{n}]\boldsymbol{n} \tag{7}$$

For the 2D stress state, $\boldsymbol{\tau}$ also only changes in magnitude, but not in direction. By changing the angle θ in 2D stress state, the analytical stress transformation equations shown below can be used to calculate the normal and shear stresses over any plane at time t:

$$\begin{cases} \sigma_n(t,\theta) = \frac{\sigma_{xx}(t)+\sigma_{yy}(t)}{2} + \frac{\sigma_{xx}(t)-\sigma_{yy}(t)}{2}\cos 2\theta + \tau_{xy}(t)\sin 2\theta \\ \\ \tau(t,\theta) = -\frac{\sigma_{xx}(t)-\sigma_{yy}(t)}{2}\sin 2\theta + \tau_{xy}(t)\cos 2\theta \end{cases} \tag{8}$$

3. Methodology

3.1. Constrained natural element method

The natural element method (NEM) uses a cloud of nodes to divide the bounded domain into a group of Voronoi cells (Braun and Sambridge, Braun and Sambridge (1995)). However, the NEM is unable to achieve linear interpolation over the non-convex boundaries. To overcome this issue, a visibility criterion is introduced into the Voronoi diagram by Yvonnet et al. (2004) to give rise to the constrained natural element method (CNEM):

$$\mathcal{V}_i^C = \left\{ a \in \Omega^D : d\left(\boldsymbol{x}, \boldsymbol{x}_i\right) \leq d\left(\boldsymbol{x}, \boldsymbol{x}_j\right) \forall j \neq i \cap a \text{ is visible from } i \text{ and } j \right\} \tag{9}$$

where $\mathcal{V}_i^C$ is the constrained Voronoi cell of node i, $\boldsymbol{x}_i$ represents the coordinates of node i and $d\left(\boldsymbol{x}, \boldsymbol{x}_j\right)$ is the Euclidean distance between node a and node j. In the visibility criterion, node a is visible from another node b if the line segment $[a, b]$ connecting them neither passes through the domain boundary Γ nor outside the domain, as shown in Fig. 5. The constrained Voronoi diagram in a 2D non-convex domain is plotted in Fig. 6.

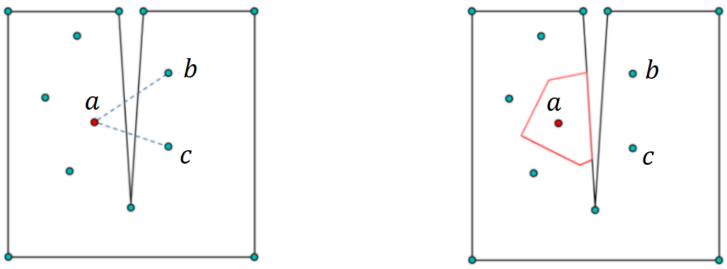

Figure 5: Visibility criterion (left) and constrained Voronoi cell of node a (right)

The constrained natural element method (CNEM) is based on the use of natural neighbor-based interpolation schemes, such as Sibson interpolation (Sibson (1981)). The Sibson interpolation function depend neither on the

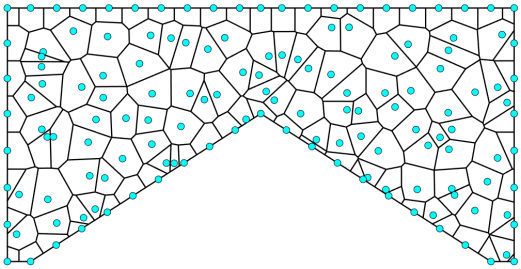

Figure 6: Constrained Voronoi diagram of a cloud of N nodes in 2D

Delaunay mesh nor on the distance to its neighbors, but is determined by the appropriate Lebesgue measure of the spatial dimensionality, as shown in Fig. 7. First, the original Voronoi diagram is locally modified by introducing a new Voronoi cell at point $\boldsymbol{x}$ (blue area). Then, the interpolation function is calculated based on geometrical considerations:

$$\phi_i(\boldsymbol{x}) = \frac{V_i(\boldsymbol{x})}{V(\boldsymbol{x})} \text{ with } V(\boldsymbol{x}) = \sum_{i=1}^{n} V_i(\boldsymbol{x}) \tag{10}$$

where $V_i(\boldsymbol{x})$ is the area of the intersection (green region) of Voronoi cell $\mathcal{V}_i^C$ (yellow region) and the new Voronoi cell $\mathcal{V}_x^C$ (blue region), $V(\boldsymbol{x})$ denotes the area of the new Voronoi cell $\mathcal{V}_x^C$, and n is the number of natural neighborhoods of point $\boldsymbol{x}$.

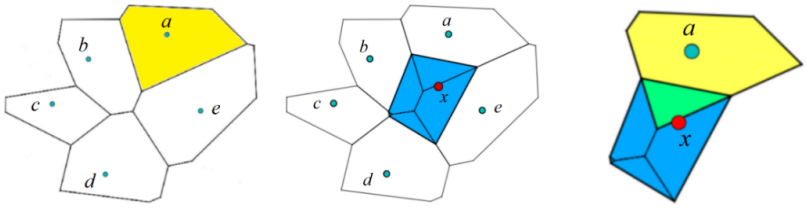

Figure 7: Process to compute Sibson interpolant in 2D

The Sibson interpolant enjoys several properties, such as the Kronecker delta property, partition of unity and linear consistency (Sukumar et al. (1998)):

$$\phi_i\left(\boldsymbol{x}_j\right) = \delta_{ij}, \quad \sum_{i=1}^{n} \phi_i(\boldsymbol{x}) = 1, \quad u(\boldsymbol{x}) = \sum_{i=1}^{n} \phi_i(\boldsymbol{x})\, u_i \tag{11}$$

where δ_{ij} is the Kronecker delta operator.

Due to the non-polynomial nature of the Sibson interpolation, it is necessary to use enough integration points to minimize the error, which makes the computation of the stiffness matrix too expensive (Chi et al. (2016)). To improve the efficiency and accuracy, the stabilized conforming nodal integration scheme (SCNI) proposed by Chen et al. (2001) is applied in this study. In SCNI, the strain smoothing stabilization is performed to stabilize the nodal integrals:

$$\bar{\boldsymbol{\varepsilon}}_i^h(\boldsymbol{x}) = \frac{1}{V_i(\boldsymbol{x})} \int_{\Omega_i} \boldsymbol{B}_i(\boldsymbol{x}) \boldsymbol{u}_i \, d\Omega \tag{12}$$

where $\boldsymbol{B}_i$ is the strain-displacement matrix of $\mathcal{V}_i^C$.

Based on the divergence theorem, Eq. 12 can be rewritten as:

$$\bar{\boldsymbol{\varepsilon}}_i^h(\boldsymbol{x}) = \frac{1}{V_i(\boldsymbol{x})} \oint_{\Gamma_i} \boldsymbol{\phi}_i(\boldsymbol{x}) \boldsymbol{u}_i \cdot \boldsymbol{n} \, d\Gamma = \bar{\boldsymbol{B}}_i(\boldsymbol{x}) \boldsymbol{u}_i \tag{13}$$

where $\bar{\boldsymbol{B}}_i$ is the average strain-displacement matrix of $\mathcal{V}_i^C$.

Then the Cauchy stress tensor can be calculated through:

$$\boldsymbol{\sigma}^h(\boldsymbol{x}) = \sum_{i=1}^{N} \boldsymbol{C} \bar{\boldsymbol{B}}_i(\boldsymbol{x}) \boldsymbol{u}_i \tag{14}$$

where $\boldsymbol{C}$ is the material constitutive matrix.

3.2. Density based topology optimization

The topology optimization for continuum structures using the solid isotropic material with penalization (SIMP) method is presented in this study. The general optimization statement can be expressed as follows:

$$\begin{aligned} &\min \; c(\boldsymbol{\rho}) = \frac{1}{|\Omega|} \sum_{i=1}^{N} \rho_i V_i \\ &\text{s.t.} \begin{cases} g_i(\boldsymbol{\rho}, \boldsymbol{u}) \leq 0, & i = 1, \dots N \\ 0 \leq \rho_j \leq 1, & j = 1, \dots N \end{cases} \\ &\text{with: } \boldsymbol{K}(\boldsymbol{\rho}) \boldsymbol{u} = \boldsymbol{f} \end{aligned} \tag{15}$$

where c is the objective function to minimize, V_i represent the volume of i-th element, $|\Omega|$ is the total volume of design domain, g_i is i-th constraint function, which depends not only on the design variable $\boldsymbol{\rho}$, but also on the displacement $\boldsymbol{u}$, N is the number of elements, $\boldsymbol{K}$ and $\boldsymbol{f}$ represent the global stiffness matrix and the external force vector respectively.

To avoid numerical instability, the polynomial filter proposed by Zegard and Paulino (2016) is used, such that $\widetilde{\boldsymbol{\rho}} = \boldsymbol{\mathcal{F}}\boldsymbol{\rho}$. The (i, j)-th component of the filter matrix $\boldsymbol{\mathcal{F}}$ is calculated as:

$$\mathcal{F}_{ij} = \frac{H_{ij}\rho_j}{\sum_{k=1}^{N} H_{ik}\rho_k}, \text{ with } H_{ij} = \max\left[0, 1 - \frac{d\left(\boldsymbol{x}_i, \boldsymbol{x}_j\right)}{R}\right]^s \tag{16}$$

where R is the radius of the filter and exponent $s \geq 1$ is the index.

To obtain a black-and-white design, the Heaviside projection function (Guest et al. (2004); Wang et al. (2011)) is applied in this study:

$$\bar{\rho}_i = \frac{\tanh(\beta\eta) + \tanh\left[\beta\left(\tilde{\rho}_i - \eta\right)\right]}{\tanh(\beta\eta) + \tanh[\beta(1-\eta)]} \tag{17}$$

where η is the projection threshold, β controls the slope of the function near the threshold parameter η.

The stiffness matrix $\boldsymbol{K}$ in Eq. 15 is calculated through a typical assembly process:

$$\boldsymbol{K}(\overline{\boldsymbol{\rho}}) = \sum_{i=1}^{N} \mathbb{A}^i \boldsymbol{K}^i, \text{ with } \boldsymbol{K}^i = \left[\epsilon + (1-\epsilon)\bar{\rho}_i^p\right] \boldsymbol{K}_0^i \tag{18}$$

where $\mathbb{A}$ is an assembly operator, $\boldsymbol{K}^i$ is the stiffness matrix of i-th element, ϵ is the Ersatz parameter to prevent singularity, p is the penalty factor, $\boldsymbol{K}_0^i$ is the stiffness matrix for $\bar{\rho}_i = 1$.

3.3. Augmented Lagrangian Method

The Augmented Lagrangian method deals with local constraints by adding them to the objective function in the form of a penalty term. The solution to the constrained optimization problem is then obtained by solving a series of unconstrained ones, each of which aims to minimize the AL function

$J(\overline{\boldsymbol{\rho}}, \boldsymbol{\lambda}, \mu)$. The unconstrained optimization problem at k-th iteration is represented as follows:

$$\min J^{(k)}(\overline{\boldsymbol{\rho}}, \boldsymbol{\lambda}, \mu) = c(\overline{\boldsymbol{\rho}}) + \frac{1}{N}\sum_{j=1}^{N}\left[\lambda_j^{(k)} h_j(\overline{\boldsymbol{\rho}}, \boldsymbol{u}) + \frac{\mu^{(k)}}{2} h_j(\overline{\boldsymbol{\rho}}, \boldsymbol{u})^2\right] \tag{19}$$

where

$$h_j(\overline{\boldsymbol{\rho}}, \boldsymbol{u}) = \max\left[g_j(\overline{\boldsymbol{\rho}}, \boldsymbol{u}), -\frac{\lambda_j^{(k)}}{\mu^{(k)}}\right] \tag{20}$$

are equality constraints, $\lambda_j^{(k)}$ is the Lagrange multiplier estimator, $\mu^{(k)} > 0$ is a penalty coefficient, both $\lambda_j^{(k)}$ and $\mu^{(k)}$ are updated at each iteration as follows (Senhora et al. (2020)):

$$\begin{aligned} \mu^{(k+1)} &= \min\left[\alpha\mu^{(k)}, \mu_{\max}\right] \\ \lambda_j^{(k+1)} &= \lambda_j^{(k)} + \mu^{(k)} h_j\left(\overline{\boldsymbol{\rho}}^{(k)}, \boldsymbol{u}\right) \end{aligned} \tag{21}$$

where $\alpha > 1$ is a constant and μ_{max} is the upper limit to prevent numerical instabilities.

In order to achieve the minimization of the function $J^{(k)}(\overline{\boldsymbol{\rho}}, \boldsymbol{\lambda}, \mu)$, the modified method of moving asymptotes (MMA) proposed by Giraldo-Londoño and Paulino (2021) is applied in this study. In each iteration, a few MMA inner loops are implemented to approximately minimize the AL function, followed by updating $\lambda_j^{(k)}$ and $\mu^{(k)}$ until the convergence is reached. Particularly, the problem has converged when $max\left(\frac{1}{N}\left|\boldsymbol{\rho}^{(k+1)} - \boldsymbol{\rho}^{(k)}\right|\right) \leq \delta$ and $max\left(\boldsymbol{g}\right) \leq \delta_s$, where δ and δ_s are the prescribed tolerance values for design variables and constraints, respectively, $\boldsymbol{\rho}^{(k+1)}$ and $\boldsymbol{\rho}^{(k)}$ are given optimal design variable vectors of two successive iterations. For details on the solving process of the approximate minimum value and the update of the design variables, please refer to Giraldo-Londoño and Paulino (2021).

Since the HCF models considered in this study are stress-based, the fatigue-driven problem shares the same difficulty as the stress-based topology optimization problem, i.e., the singular optima due to stress singularity.

The Singular optima refers to the local optima are located in a degenerate region of the design space that is not accessible to gradient-based optimizer (Rozvany (1996); Verbart et al. (2017)). To circumvent this problem, several relaxation techniques such as ϵ-relaxation (París et al. (2009)) and qp approach (Bruggi (2008)) were proposed to perturb the degenerate space so that the singular optima can be reached by the optimizer. By analyzing different types of constraint relaxations, Chen et al. (2023) found that the polynomial vanishing constraint not only preserves the properties of the original constraint, but also allows the result to converge to the global optimum. Therefore, the original constraint function in Eq. 15 is replaced by the polynomial vanishing constraint:

$$\widetilde{g}_i(\overline{\boldsymbol{\rho}}) = [\epsilon + (1-\epsilon)\bar{\rho}_i^p]\, g_i \left(g_i^2 + 1\right) \tag{22}$$

4. Numerical results

This section presents several numerical results to demonstrate the properties of the proposed method. Table 2 shows the parameters used in this study, which apply to all examples if not otherwise specified. The mechanical and fatigue parameters correspond to additive manufactured Ti-6Al-4V alloy (Mower and Long (2016); Fatemi et al. (2017)). This material is considered to be homogeneous, isotropic and linearly elastic. Each individual load applied in this paper is constant amplitude cyclic load with stress ratio $\sigma_{min}/\sigma_{max} = -1$. According to the definition of the HCF model, the effect of load frequency on fatigue life is negligible. Furthermore, the fatigue damage during one cycle and multiple cycles is consistent in the calculations. Therefore, the fatigue criteria can be evaluated for only one load cycle. In the 2D problems given below, plane stress condition is assumed.

4.1. 2D L-bracket under single load

Firstly, the topology optimization problem of a 2D L-bracket under a single load is considered. The design domain and boundary conditions is shown in Fig. 8. The model is fully constrained at the upper left edge and the distributed load $\boldsymbol{f}$ is applied along the distance d to the upper right free end. The geometry and loading conditions are shown in Table 3. The HCF criteria listed in Table 1 involve the calculation of stress amplitudes, mean values, and maximum values during the load cycle. Since this study considers

Table 2: Input parameters used in this study

Parameter	Description	Value
$\boldsymbol{\rho}^{(0)}$	Initial density vector	$\mathbf{0.5}$
β	Initial Heaviside projection penalization factor	1
$\beta_{\max}$	Maximum Heaviside projection penalty factor	10
η	Heaviside projection threshold	0.5
$\boldsymbol{\lambda}^{(0)}$	Initial Lagrange multiplier vector	$\mathbf{0}$
$\mu^{(0)}$	Initial penalty coefficient	10
α	Penalty factor updating parameter	1.05
q	Nonlinear filter index	3.5
δ	Convergence tolerance of design variables for AL	0.005
δ_s	Convergence tolerance of stress constraints for AL	0.005
m	move limit	0.15
$MaxIter$	Maximum number of external loops	150
$MaxInAL$	Maximum number of internal loops per AL step	5
E_0	Young's modulus	108.8 GPa
ν	Poisson's ratio	0.29
$\overline{\sigma}$	Yield stress	972 MPa
σ_{ult}	Ultimate tensile stress	1034 MPa
f_{-1}	Fully reversed bending fatigue limit	454 MPa
t_{-1}	Fully reversed torsional fatigue limit	300 MPa
T	Period of cyclic load	1 s
$\Delta\theta$	Increment of angle θ	1°

the linear elasticity model, it is only necessary to focus on the stress states under the maximum and minimum loads (red dots in Fig. 8) in the case of single or proportional loading, thus avoiding high computational costs when faced with a large number of loading sequences.

The design domain is discretized with 40501 uniformly distributed nodes, and the topologies under different HCF criteria constraints are plotted in Fig. 9. It can be seen that the fatigue constraint can be satisfied anywhere according to the normalized constraint maps, where the constraint is divided by the parameter β. The optimization iterations are run by MATLAB R2021a on a computer equipped with a 2.60 GHz processor and the time consumed by the

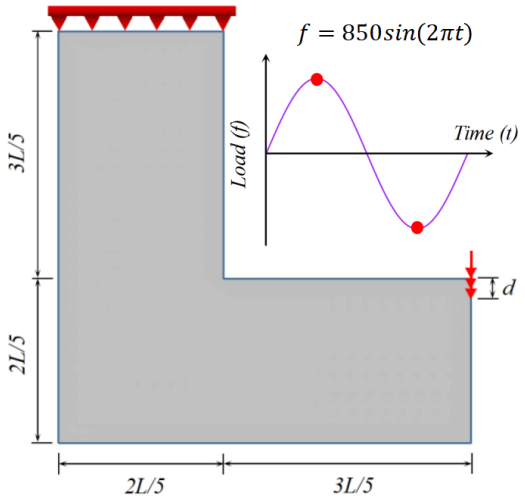

Figure 8: 2D L-bracket under single load

Table 3: Parameters for 2D L-bracket

Parameter	Description	Value
L	Length	100 mm
t	Thickness	1 mm
f	Load amplitude	850 N
d	Load distribution distance	6 mm

main loop is shown in Table 4. Since Matake and Findley require more iterations to satisfy the convergence criteria, they consume more time. It is worth mentioning that the topology optimization results based on different HCF criteria result in relatively close contours under a single load, and even, they are close to the results with von Mises stress constraints under static loading (Giraldo-Londoño and Paulino (2021)). However, this property disappears when the boundary conditions are changed.

When the HCF criteria are considered in topology optimization, the von Mises stress constraints are also satisfied and produce stress distributions that are much lower than the yield stress of the material. Relative to the Sines fatigue criterion, the result under the Crossland criterion is more secure and also has lower von Mises stresses due to the consideration of the maximum hydrostatic stress. It is worth noting that although the objective functions

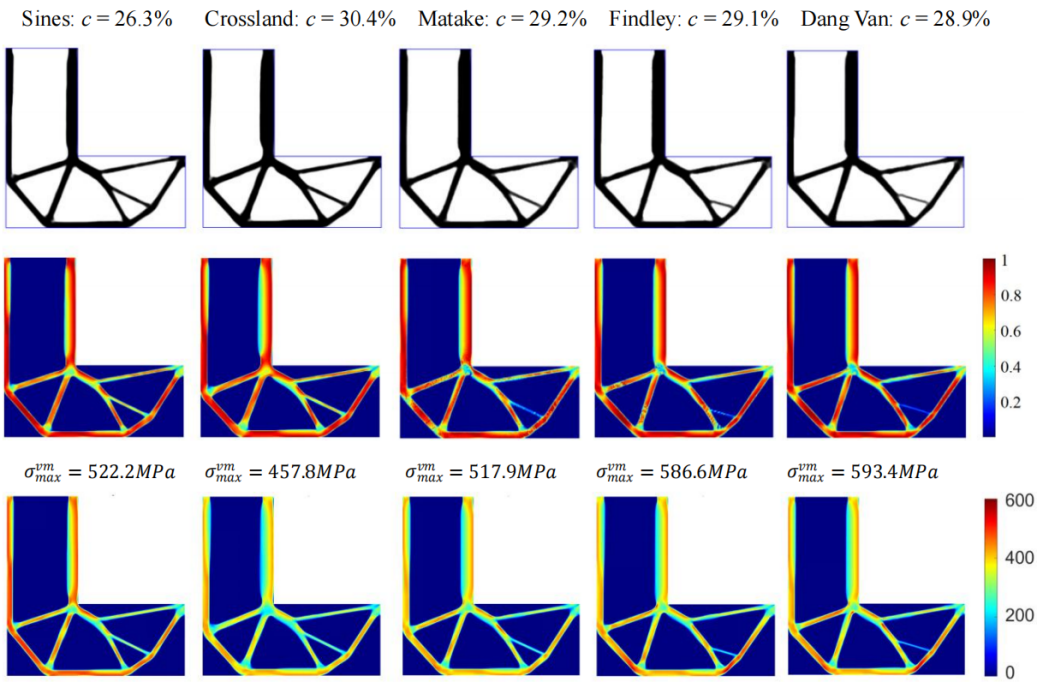

Figure 9: L-bracket topologies (top), normalized fatigue constraint (middle) and von Mises stress (bottom) maps

based on the critical plane fatigue criteria constraints are very close, the structures subjected to Findley and Dang Van criteria produce much higher von Mises stresses than Matake.

Table 4: Computation time of topology optimization main loop

HCF criteria	Sines	Crossland	Matake	Findley	Dang Van
Time (seconds)	383	329	405	448	361

4.2. 2D L-bracket under bi-axial loading

The topology optimization problem of the previous benchmark is modified by replacing single load with bi-axial loading which are located at the upper and right edges, as shown in Fig. 10. The symmetric constraints are applied at the left and lower sides. This example follows the input parameters established for the 2D L-bracket in Table 2, except that the load is adjusted to

2550N. In addition to proportional loading, the topology optimization problem subjected to HCF criteria constraints under non-proportional loading is also investigated.

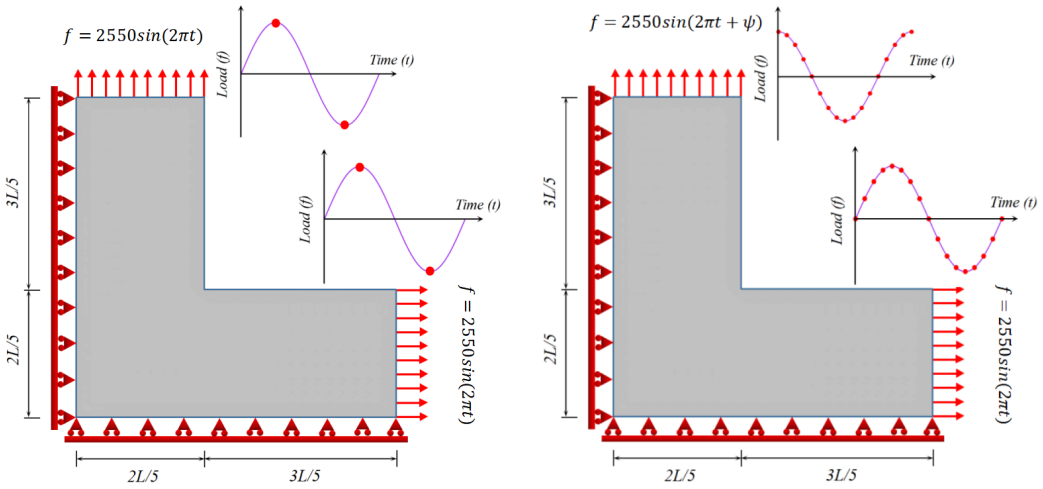

Figure 10: 2D L-bracket under proportional (left) and non-proportional (right) bi-axial loading

Under non-proportional loading, the time point when the stress vector reaches its extreme value is no longer as straightforward as proportional loading, and in order to reduce the error, it is necessary to select as many different time points as possible to calculate the amplitude, mean and maximum values of the stress during the load cycle. Therefore, 17 uniformly distributed time points are selected in this study, see Fig. 10. Hence, the non- proportional loading leads to a significant increase in computational cost relative to topology optimization that only considers proportional loading.

The topology optimization results under proportional bi-axial loading subjected to the HCF criteria constraints are presented in Fig. 11, and it can be observed that the topologies are highly dependent on the selection of the fatigue criteria. The contours with the stress-invariant fatigue criteria constraints exhibit similar structures. However, for the fatigue criteria constraints based on the critical plane, they show a big difference, not only in the branching structure near the loading positions, but also in the supporting structure near the concave corner. The topologies show several gray areas near the loaded regions, which can be improved by changing the input parameters such as filter radius, maximum Heaviside projection penalty factor,

or post-processing, but this issue is not the focus of this study.

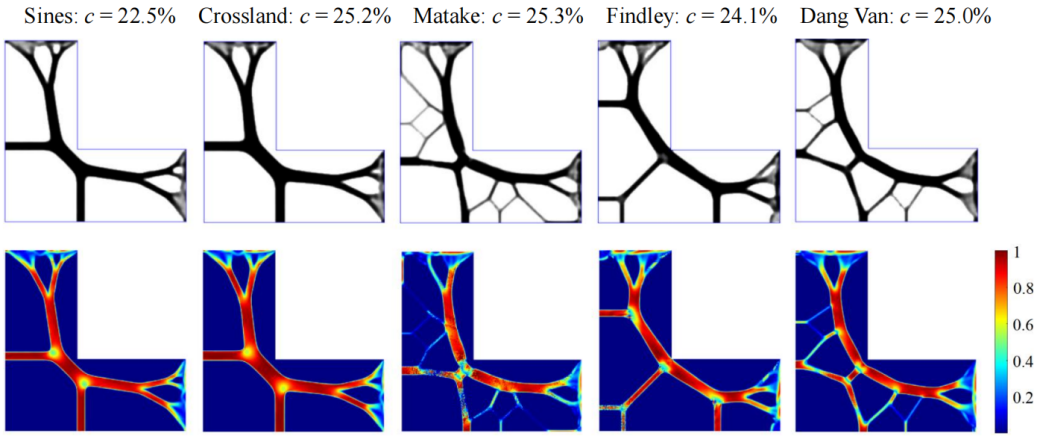

Figure 11: L-bracket topologies and normalized constraint maps under proportional bi-axial loading

When the phase difference ψ is equal to $\pi/4$ or $\pi/2$, all the topologies exhibit a cross-shaped structure near the concave corner, as shown in Fig. 12. The constraint values located at the center of the cross-connection has lower values under the first kind of criteria (yellow area) and higher values for the second kind of criteria (red area). However, when the phase difference continues to increase up to $3\pi/4$, only the results subjected to the Crossland constraints retain the above properties. Furthermore, the results under Sines and Crossland constraints do not usually differ significantly depending on the hydrostatic stress term, and also show a completely different structure under large phase difference. It is also observed that the objective function increases with increasing phase difference. Finally, due to the symmetry of the geometry and boundary conditions, all results are distributed roughly symmetrically along the diagonal of the design domain.

In order to investigate the effect of angular increments on the critical plane search, five different increment values of 0.1°, 1°, 2°,5° and 10° are selected for topology optimization. The corresponding results with Dang Van criterion constraints for a non-proportional load of $\psi = \pi/2$ are plotted in Fig. 13. Meanwhile, a density error coefficient is introduced:

$$e = \frac{\|\boldsymbol{\rho} - \boldsymbol{\rho}(\Delta\theta = 0.1°)\|}{\|\boldsymbol{\rho}(\Delta\theta = 0.1°)\|} \tag{23}$$

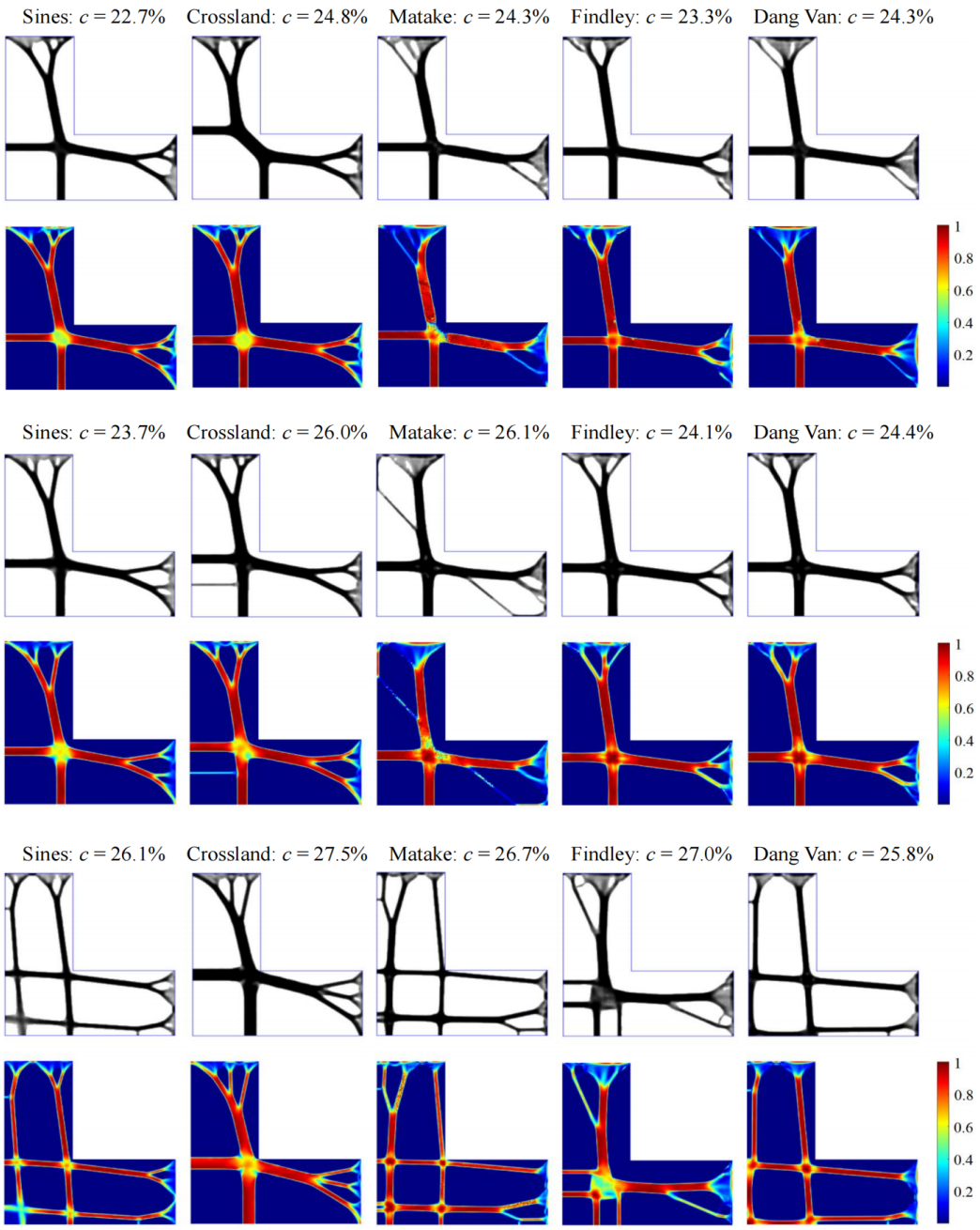

Figure 12: L-bracket topologies and normalized constraint maps under non-proportional bi-axial loading when $\psi = \pi/4$ (top), $\psi = \pi/2$ (middle) and $\psi = 3\pi/4$ (bottom)

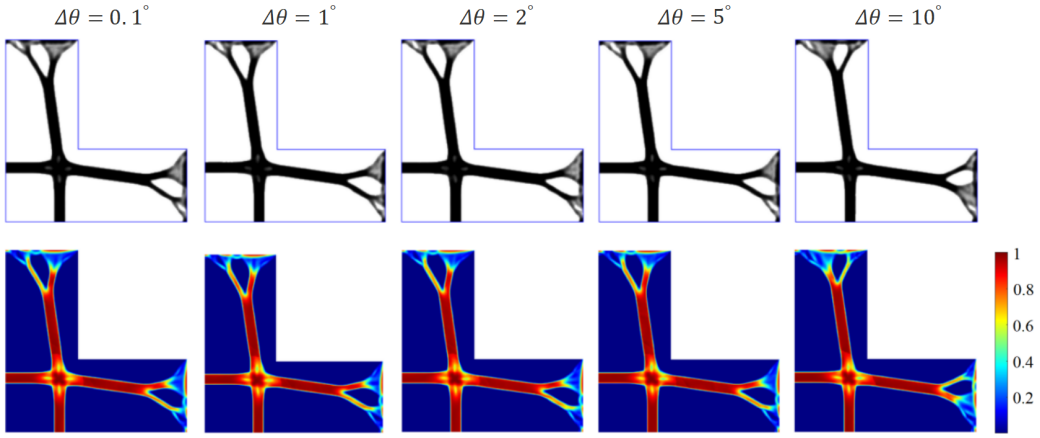

Figure 13: L-bracket topologies and normalized constraint maps with Dang Van criterion constraints under different angular increments

It can be noticed from Fig. 14 that when the angular increment is less than or equal to 2 degrees, the error is ensured to be within 10 % compared with the result of 0.1 degrees, and the overall structure does not change much. The above differences are also caused by the fact that the topology optimization problem with fatigue constraints is non-convex and there are a lot of local minima. A similar phenomenon is found under the Findley and Matake criteria constraints.

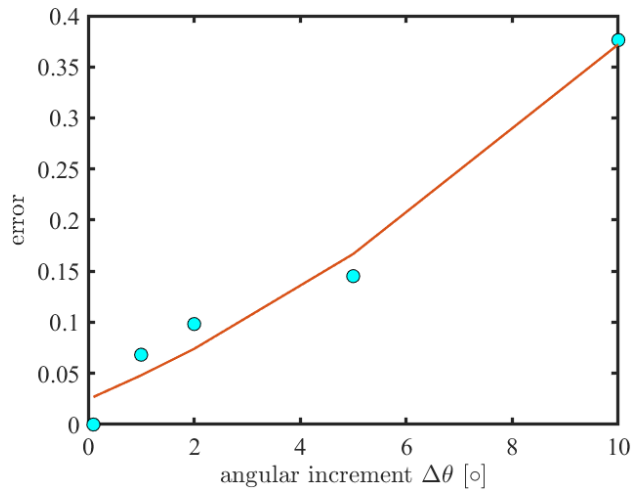

Figure 14: The relationship between angular increment and error

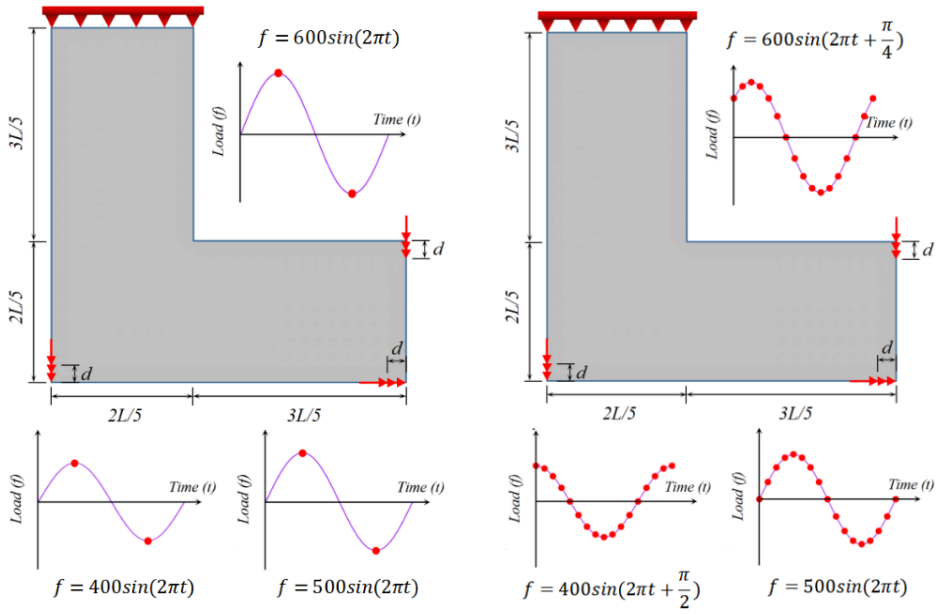

Figure 15: 2D L-bracket under proportional (left) and non-proportional (right) multiple loads

4.3. 2D L-bracket under multiple loads

The topology optimization problem of the 2D L-bracket is extended to the multi-load condition, including proportional and non-proportional loads. Unlike the previous cases, the amplitude varies for each load as well as the phase difference in non-proportional loading is different, see Fig. 15. The magnitudes of the three loads are $400N$, $500N$, and $600N$, respectively. The corresponding topologies are shown in Fig. 16. When dealing with non-proportional loading, 17 uniformly distributed time points are choose to calculate the stress values along the lines of Section 4.2.

Under proportional multiple loading, all structures show the diagonal crossbar connection structure in the upper left position, whereas the optimization results based on the stress-invariant fatigue criteria lose this property when the loading becomes non-proportional, and the outputs based on the critical plane all retain this property. Similar to the results in Section 4.1, the critical plane approaches show two branching rods in the lower right. However, for the results based on stress-invariant criteria, only one rod support is shown under both loads.

In order to verify the applicability of the results under each of the HCF

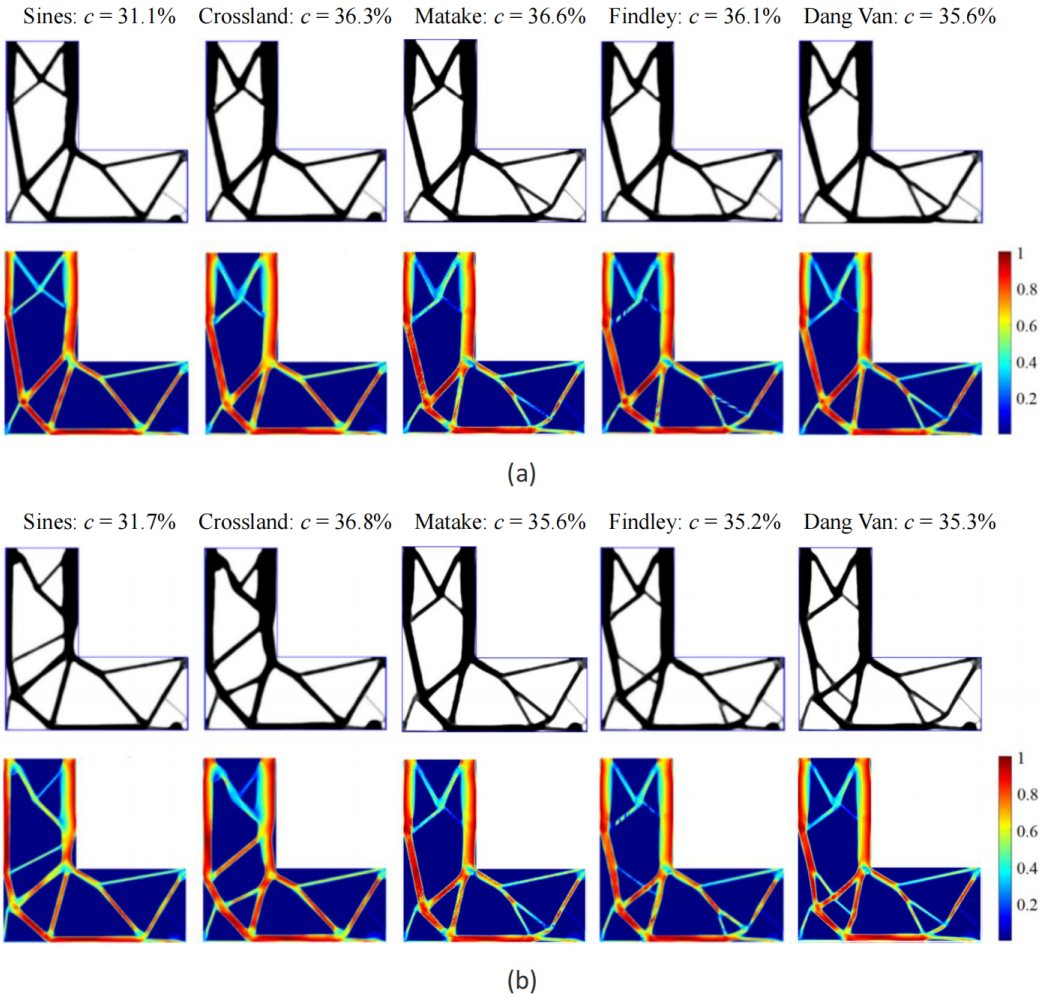

Figure 16: L-bracket topologies and normalized constraint maps under (a) proportional and (b) non-proportional multiple loads

criterion constraints to the other criteria, the results of the cross-checks under non-proportional loading are plotted in Fig. 17. The normalized maximum constraint values are displayed in Table 5. For the first category of criteria, the result under the Sines constraints violates all other criteria. However, the Crossland result satisfies almost all other criteria except for a slight violation of the Matake criterion, and vice versa, the topology under Matake criterion only violates the Crossland criterion slightly. Among the results of the second type of criteria, except for the Matake criterion, which meets

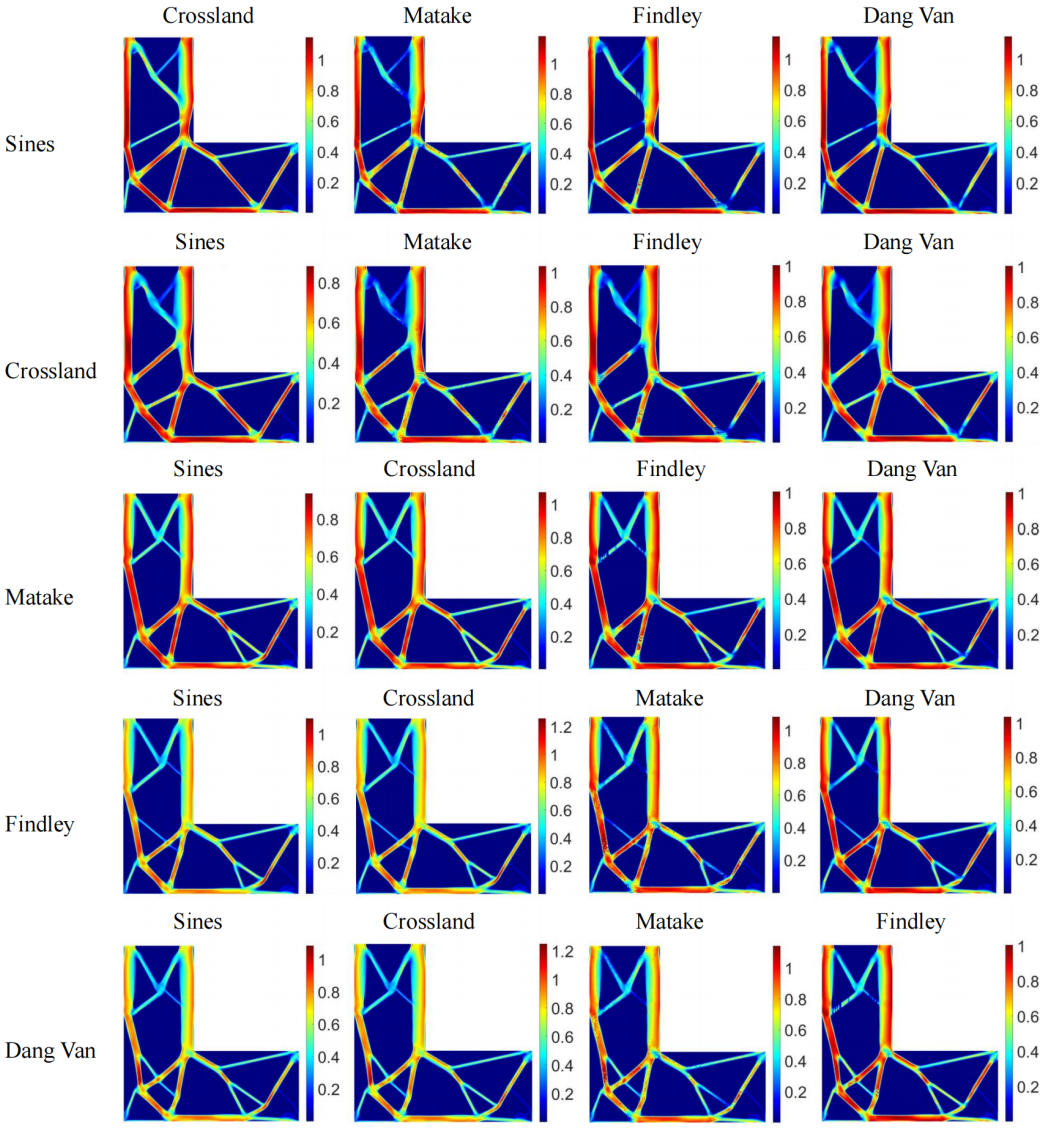

Figure 17: Cross-check of results under different fatigue criteria constraints

the Sines criterion, they all violate the first type of criteria, and in particular Findley and Dang Van severely violate the Crossland criterion. Similar to the Sines criterion, the result of Findley does not satisfy the rest of the criteria. Dang Van could satisfy Findley, but violates the Matake criterion. When the proportional loading case is analyzed, similar results are obtained.

Table 5: Normalized maximum constraint values under different fatigue criteria

Computation \ Test	Sines	Crossland	Matake	Findley	Dang Van
Sines	——	1.15	1.18	1.15	1.15
Crossland	0.88	——	1.04	1.00	1.00
Matake	0.94	1.07	——	1.00	1.00
Findley	1.01	1.26	1.08	——	1.04
Dang Van	1.08	1.25	1.14	1.00	——

4.4. 2D portal frame

The geometry and boundary conditions of the 2D portal frame is shown in Fig. 18. The parameters applied for this benchmark are listed in Table 6. When regular design domains and structured meshes are used, mesh sensitivity can be suppressed with the imposition of a larger filtering domain. An interesting aspect of this problem is that its geometry is non-convex and can therefore be used to check mesh dependence. The domain is discretized using three different numbers of elements, which are 59454, 92809 and 133484 respectively. Furthermore, for each particular number of elements, three different discretization schemes are used, i.e., regular, slightly irregular and severely irregular. In order to obtain symmetric solutions, the design variables on the left and right sides of the two programs are symmetrized during the optimization.

Table 6: Parameters for 2D portal frame

Parameter	Description	Value
L	Length	120 mm
H	Height	60 mm
h	Concave height	35 mm
b	Bearing length	5.5 mm
t	Thickness	1 mm
f	Load amplitude	1400 N
d	Load distribution distance	10 mm

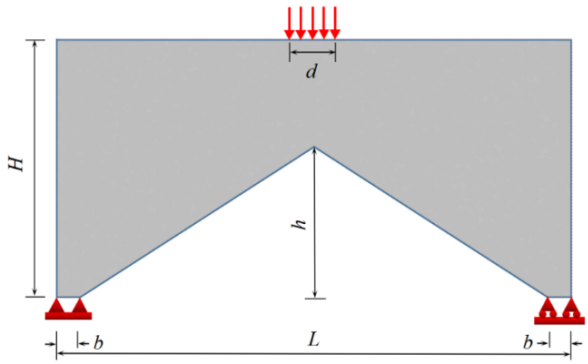

Figure 18: Design domain and boundary conditions of 2D portal frame problem

Since the mesh sensitivity problem does not arise in any of the arithmetic cases, only the topologies and normalized constrained maps subject to Dang Van fatigue criterion constraints are plotted in Fig. 19. It can be noticed that the optimization results are not only independent of mesh encryption but also of mesh quality, only the irregular discretization scheme leads to the thickness of several staffs slightly increased. This is the advantage of CNEM over the commonly used finite element method. Nevertheless, the construction of the interpolation function in CNEM requires more neighbor nodes, resulting in larger strain-displacement matrix and wider stiffness matrix bandwidth, which consumes more time in equilibrium equation solving and sensitivity analysis.

The finite element method has a great speed advantage in dealing with regular design domains for topology optimization, but in non-regular geometries, a series of iterations are required to generate a high quality mesh during the pre-processing stage and the relationship between the number of iterations and the optimization results is still not clear. Therefore, the method proposed in this paper is expected to stableachieve stable output under various discretization schemes for topology optimization problems with HCF criteria constraints.

5. Discussion

In topology optimization, all criteria show similar predictions under a single load. However, in the case of complex loads and non-proportional loading, different fatigue criteria usually lead to different predictions. For the criteria

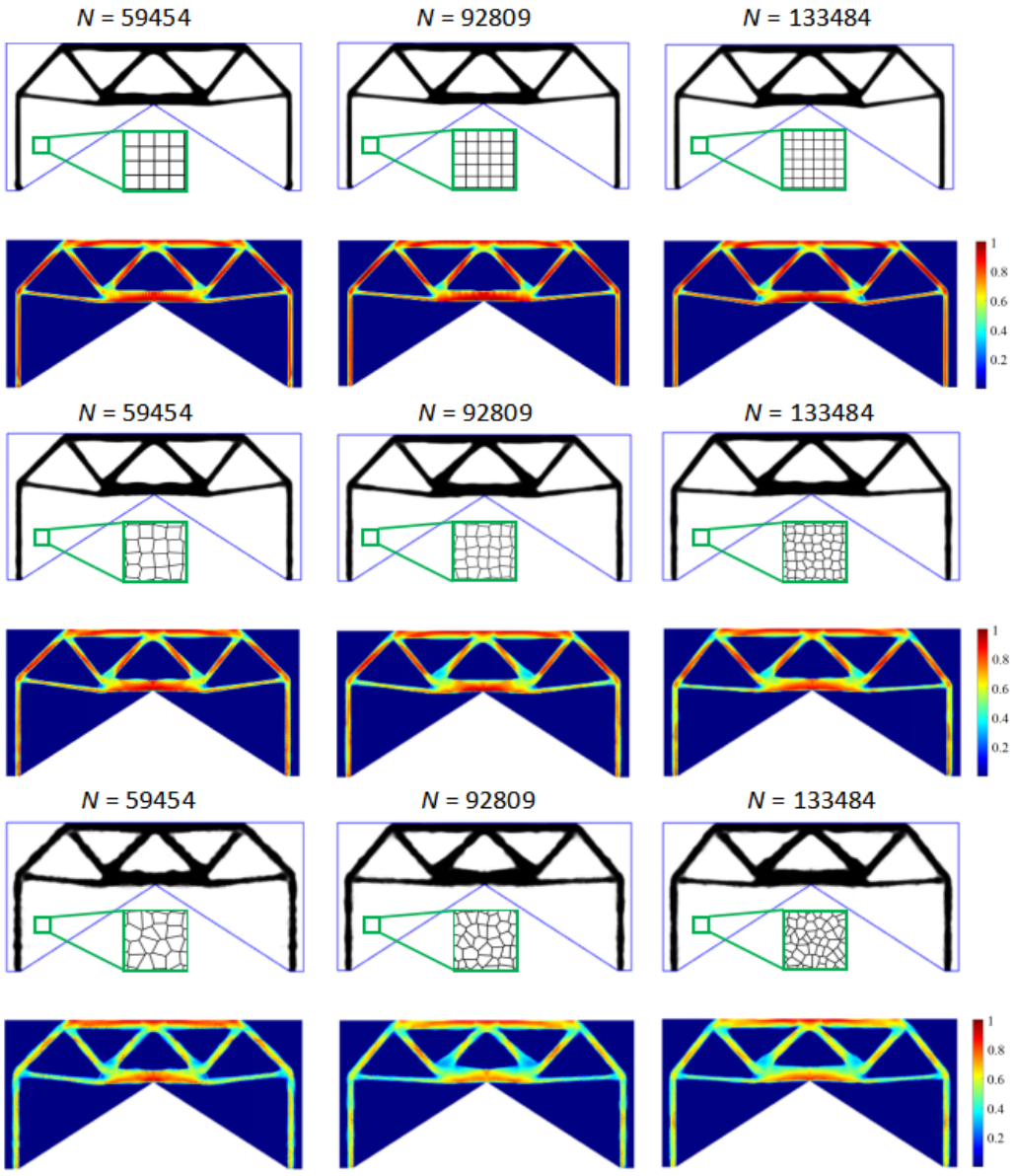

Figure 19: Topologies and normalized Dang Van constraint maps for several discretization schemes

based on the stress invariant, the Crossland criterion is favored over the Sines criterion in industry since the maximum hydrostatic stress typically leads to more conservative predictions than its mean value. Although the predictions

of Crossland under uni-axial and bi-axial stress states are not as conservative as that critical plane based criteria, it exhibits a more conservative prediction in multi-axial stress states, and its results satisfy almost all other fatigue criteria. This phenomenon is consistent with the fatigue experimental results obtained by Sahadi et al. (2017): the Crossland criterion conformed best to the experimental data, while the critical plane criteria gave conservative predictions for the uni-axial stress case and non-conservative predictions for multi-axial conditions. The Sines criterion always seems to give the most aggressive predictions, due to the fact that its second stress term $\sigma_{H,mean}$ is null when the mean stress is not considered. As a result, topology optimization results subject to the Sines criterion usually have a small objective function and cannot satisfy the other criteria simultaneously.

For the criteria based on critical plane, the Matake and Findley prediction curves are almost parallel under single cases, while the predictions of Matake are more conservative. In fact, the Matake criterion has been always the most conservative under simple cases. Based on the topology optimization results under multiple loads, the Matake gives the most conservative predictions, and it seems to be able to satisfy other criteria as well. This performance is similar to Crossland. In paticular, the topology optimization results of Matake and Crossland only slightly violate each other, and the objective functions of both are usually the largest. Since only the shear stress amplitude is used to determine the critical plane, the result of Dang Van meets Findley, but not vice versa. Therefore, it seems more reasonable to use only shear stress to determine the critical plane. The above conclusions are also consistent with the experimental results in the references (Papadopoulos et al. (1997); Sahadi et al. (2017)), where the Matake is an improvement over Findley and gives the most conservative prediction for uni-axial stress conditions.

In this study, only a few very classical and common multi-axial HCF criteria are considered. However, these classical fatigue criteria may be inefficient in accurately describing the fatigue behavior under non-proportional loading (Papadopoulos et al. (1997); Pejkowski (2017)). The fatigue behavior of many materials under non-proportional loading conditions is significantly different from that under proportional loading conditions (Skibicki and Pejkowski (2019)). Therefore, a large number of multi-axial fatigue models have been developed for non-proportional loading, in which more material parameters are added to account for material sensitivity to non-proportionality of fatigue loading. For the description and discussion of these fatigue criteria, please refer to Pejkowski (2017). Note that additional fatigue experiments

are required to implement these fatigue criteria for non-proportional loading, and their applicability is still not widely proven.

Topology optimization aims at obtaining a reasonable initial design, and the optimized structure needs to be geometrically reshaped by post-processing software before manufacturing (Zegard and Paulino (2016)). Subedi et al. (2020) gave an overview of geometric post-processing methods for topology optimization models, e.g., skeleton extraction, surface fitting, volume decomposition and so on. For some details, such as the surfaces with small curvature radius will be smoother and easier to manufacture after reconstruction. Subsequently, the reshaped model needs to be further validated by fatigue tests.

6. Conclusion and perspective

This study uses CNEM to solve equilibrium equations and AL approach to solve local minima problems. Due to the properties of CNEM, it becomes possible to obtain stable outputs under different discretization schemes and rapid discretization of complex design domain is realistic. Furthermore, since the AL formulation requires only one adjoint vector for each load under non-proportional loading (simplified to one adjoint vector under proportional loading), yielding an effective sensitivity analysis. As a result, it can significantly reduce the costs associated with a large number of constraints while providing a more consistent model than the aggregation technique, i.e. the constraints are locally satisfied.

The rational choice of HCF model under complex loading should be prudent, which may depends on the material and load characteristics. Especially under non-proportional loading, when the phase difference is large, the topology optimization results predicted by different criteria can be very different. Metal additive manufacturing parts usually undergo a complex cyclic thermal history including directional heat extraction, repetitive melting, and rapid solidification, which produces anisotropic and heterogeneous micro-structures that are fundamentally different from those of metal parts fabricated via conventional methods. The presence of defects such as porosity, surface roughness and unfusion also induce anisotropy and heterogeneity in metal additive manufacturing parts. Therefore, the future work includes considering the additive manufacturing constraints in topology optimization, since the fatigue behavior can be affected by the rough build surfaces and defects introduced in the manufacturing process. Then the topology opti-

mization problem under the constraint of HCF criteria can be extended to 3D applications, and the accuracy of each criterion in predicting fatigue life can be validated through fatigue tests. In addition, the fatigue criteria that take into account stress gradients and stress concentration effects should be attempted.

7. Conflict of interest statement

On behalf of all authors, the corresponding author states that there is no conflict of interest.

8. Acknowledgments

The authors acknowledge the financial support from "China Scholarship Council (CSC)" under the project titled "Topology optimization of additive manufactured parts including fatigue behavior", Grant No. 202008310112.

Appendix A. Sensitivity analysis

In order to apply the gradient-based optimizer, the sensitivity of the AL function in Eq. 19 need to be calculated:

$$\frac{\partial J}{\partial \rho_i} = \sum_{j=1}^{N} \left(\frac{\partial c}{\partial \tilde{\rho}_j} \frac{d\tilde{\rho}_j}{d\rho_i} + \frac{1}{N} \frac{\partial P}{\partial \tilde{\rho}_j} \frac{d\tilde{\rho}_j}{d\rho_i} \right) \tag{A.1}$$

where

$$P^{(k)}(\overline{\boldsymbol{\rho}}, \boldsymbol{u}) = \sum_{j=1}^{N} \left[\lambda_j^{(k)} h_j(\overline{\boldsymbol{\rho}}, \boldsymbol{u}) + \frac{\mu^{(k)}}{2} h_j(\overline{\boldsymbol{\rho}}, \boldsymbol{u})^2 \right] \tag{A.2}$$

is the penalization term.

The derivative of the objective function c to the i-th design variable is calculated as follows:

$$\frac{\partial c}{\partial \tilde{\rho}_i} = \frac{\partial}{\partial \tilde{\rho}_i} \frac{\sum_{j=1}^{N} \bar{\rho}_j V_j}{|\Omega|} = \frac{V_i}{|\Omega|} \frac{d\bar{\rho}_i}{d\tilde{\rho}_i} = \frac{V_i}{|\Omega|} \frac{\beta \left[1 - \tanh\left(\beta\left(\tilde{\rho}_i - \eta\right)\right)\right]^2}{\tanh(\beta\eta) + \tanh[\beta(1-\eta)]} \tag{A.3}$$

The derivative of the penalization term P to the i-th design variable is expressed as:

$$\frac{\partial P^{(k)}}{\partial \tilde{\rho}_i} = \sum_{j=1}^{N} \left[\left(\lambda_j^{(k)} + \mu^{(k)} h_j \right) \left(\frac{\partial h_j}{\partial \tilde{\rho}_i} + \frac{\partial h_j}{\partial \boldsymbol{u}} \frac{\partial \boldsymbol{u}}{\partial \tilde{\rho}_i} \right) \right] \tag{A.4}$$

In order to avoid calculating the derivatives of the displacements with respect to the design variables, the adjoint method is used here to simplify the calculation:

$$\widehat{P}^{(k)} = P^{(k)} + \sum_{l=1}^{n_f} \left[\boldsymbol{\eta}_l^T \left(\boldsymbol{K} \boldsymbol{u}_{l,ref} - \boldsymbol{f}_{l,ref} \right) \right] \tag{A.5}$$

Then Eq. A.4 can be replaced by:

$$\frac{\partial \widehat{P}^{(k)}}{\partial \tilde{\rho}_j} = \frac{\partial P^{(k)}}{\partial \tilde{\rho}_j} + \sum_{l=1}^{n_f} \boldsymbol{\eta}_l^T \frac{\partial \boldsymbol{K}}{\partial \tilde{\rho}_j} \boldsymbol{u}_{l,ref} \tag{A.6}$$

with the adjoint equation:

$$\boldsymbol{\eta}_l = -\boldsymbol{K}^{-T} \left[\frac{\partial P^{(k)}}{\partial \boldsymbol{u}_{l,ref}} \right]^T = -\boldsymbol{K}^{-T} \left\{ \sum_{j=1}^{N} \left[\left(\lambda_j^{(k)} + \mu^{(k)} h_j \right) \left(\frac{\partial h_j}{\partial \boldsymbol{u}_{l,ref}} \right) \right] \right\}^T \tag{A.7}$$

The first item $\partial \widehat{P}^{(k)} / \partial \tilde{\rho}_j$ in Eq. A.6 is determined as:

$$\frac{\partial P}{\partial \widetilde{\rho}_i} = \left(\lambda_i^{(k)} + \mu^{(k)} h_i \right) p(1-\epsilon) \bar{\rho}_i^{(p-1)} g_i \left(g_i^2 + 1 \right) \tag{A.8}$$

and the item $\partial h_j / \partial \boldsymbol{u}_{l,ref}$ for different HCF criteria can be calculated as:

$$\begin{aligned} \text{Sines:} \qquad \frac{\partial h_j}{\partial \boldsymbol{u}_{l,ref}} &= \frac{\partial h_j}{\partial \sqrt{J_{2,a}^j}} \frac{\partial \sqrt{J_{2,a}^j}}{\partial \boldsymbol{\sigma}_a} \frac{\partial \boldsymbol{\sigma}_a}{\partial \boldsymbol{\sigma}_{l,ref}} \frac{\partial \boldsymbol{\sigma}_{l,ref}}{\partial \boldsymbol{u}_{l,ref}} \\ &+ \frac{\partial h_j}{\partial \sigma_{H,mean}^j} \frac{\partial \sigma_{H,mean}^j}{\partial \boldsymbol{\sigma}_{mean}^j} \frac{\partial \boldsymbol{\sigma}_{mean}^j}{\partial \boldsymbol{\sigma}_{l,ref}} \frac{\partial \boldsymbol{\sigma}_{l,ref}}{\partial \boldsymbol{u}_{l,ref}} \end{aligned} \tag{A.9}$$

$$\text{Crossland:}\quad \frac{\partial h_j}{\partial \boldsymbol{u}_{l,ref}} = \frac{\partial h_j}{\partial \sqrt{J^j_{2,a}}} \frac{\partial \sqrt{J^j_{2,a}}}{\partial \boldsymbol{\sigma}_a} \frac{\partial \boldsymbol{\sigma}_a}{\partial \boldsymbol{\sigma}_{l,ref}} \frac{\partial \boldsymbol{\sigma}_{l,ref}}{\partial \boldsymbol{u}_{l,ref}} + \frac{\partial h_j}{\partial \sigma^j_{H,max}} \frac{\partial \sigma^j_{H,max}}{\partial \sigma^j_{Hl,ref}} \frac{\partial \sigma^j_{Hl,ref}}{\partial \boldsymbol{\sigma}_{l,ref}} \frac{\partial \boldsymbol{\sigma}_{l,ref}}{\partial \boldsymbol{u}_{l,ref}} \tag{A.10}$$

$$\text{Matake/Findley:}\quad \frac{\partial h_j(\theta)}{\partial \boldsymbol{u}_{l,ref}} = \frac{\partial h_j(\theta)}{\partial \tau^j_a(\theta)} \frac{\partial \tau^j_a(\theta)}{\partial \boldsymbol{\tau}_{l,ref}(\theta)} \frac{\partial \boldsymbol{\tau}_{l,ref}(\theta)}{\partial \boldsymbol{\sigma}_{l,ref}} \frac{\partial \boldsymbol{\sigma}_{l,ref}}{\partial \boldsymbol{u}_{l,ref}} + \frac{\partial h_j(\theta)}{\partial \sigma^j_{n,\max}(\theta)} \frac{\partial \sigma^j_{n,\max}(\theta)}{\partial \boldsymbol{\sigma}_{nl,ref}(\theta)} \frac{\partial \boldsymbol{\sigma}_{nl,ref}(\theta)}{\partial \boldsymbol{\sigma}_{l,ref}} \frac{\partial \boldsymbol{\sigma}_{l,ref}}{\partial \boldsymbol{u}_{l,ref}} \tag{A.11}$$

$$\text{Dang Van:}\quad \frac{\partial h_j(\theta)}{\partial \boldsymbol{u}_{l,ref}} = \frac{\partial h_j(\theta)}{\partial \tau^j_a(\theta)} \frac{\partial \tau^j_a(\theta)}{\partial \boldsymbol{\tau}_{l,ref}(\theta)} \frac{\partial \boldsymbol{\tau}_{l,ref}(\theta)}{\partial \boldsymbol{\sigma}_{l,ref}} \frac{\partial \boldsymbol{\sigma}_{l,ref}}{\partial \boldsymbol{u}_{l,ref}} + \frac{\partial h_j}{\partial \sigma^j_{H,max}} \frac{\partial \sigma^j_{H,max}}{\partial \sigma^j_{Hl,ref}} \frac{\partial \sigma^j_{Hl,ref}}{\partial \boldsymbol{\sigma}_{l,ref}} \frac{\partial \boldsymbol{\sigma}_{l,ref}}{\partial \boldsymbol{u}_{l,ref}} \tag{A.12}$$

The non-zero sensitivities of the $\boldsymbol{h}$ function to the stress invariant of j-th node are:

$$\begin{cases} \frac{\partial h_j}{\partial \sqrt{J^j_{2,a}}} = \frac{\partial h_j}{\partial \tau^j_a} = \frac{p(1-\epsilon)\bar{\rho}^{(p-1)}_j \left(3g^2_j+1\right)}{\beta} \\ \frac{\partial h_j}{\partial \sigma^j_{H,\max}} = \frac{\partial h_j}{\partial \sigma^j_{n,\max}} = \frac{\alpha p(1-\epsilon)\bar{\rho}^{(p-1)}_j \left(3g^2_j+1\right)}{\beta} \end{cases} \tag{A.13}$$

when $\widetilde{g}_i(\overline{\boldsymbol{\rho}}) \geq -\lambda^{(k)}_i/\mu^{(k)}$, otherwise $\partial h_j/\partial \boldsymbol{u}_{l,ref} = 0$.

The calculation based on the Sines criteria can be simplified under cyclic loading with a stress ratio of -1 due to $\boldsymbol{\sigma}_{H,mean} \equiv 0$ and $\partial h_j/\partial \boldsymbol{\sigma}^j_{mean} \equiv 0$.

The derivative of $\sqrt{J^j_{2,a}}$ to the amplitude of Cauchy stress vector is equal to:

$$\frac{\partial \sqrt{J^j_{2,a}}}{\partial \boldsymbol{\sigma}_a} = \frac{\boldsymbol{M}\boldsymbol{\sigma}_a}{\sqrt{J^j_{2,a}}} \tag{A.14}$$

Based on Eq. 5, the derivatives of the shear stress amplitude and maximum normal stress with respect to the stress vector over the critical plane under the l-th unit load are:

$$\begin{cases} \frac{\partial \boldsymbol{\tau}_a(\boldsymbol{\theta})}{\partial \boldsymbol{\tau}_{l,ref}(\boldsymbol{\theta})} = \frac{1}{2}\left(\boldsymbol{c}_{\tau l,max} - \boldsymbol{c}_{\tau l,min}\right) \\ \\ \frac{\partial \boldsymbol{\sigma}_{n,max}(\boldsymbol{\theta})}{\partial \boldsymbol{\sigma}_{nl,ref}(\boldsymbol{\theta})} = \boldsymbol{c}_{nl,max} \end{cases} \tag{A.15}$$

As in Eq. 5, the maximum hydrostatic stress and normal stress under non-proportional loading can also be calculated through:

$$\boldsymbol{\sigma}_{H,max}(\boldsymbol{x},t) = \sum_{l=1}^{n_f} \boldsymbol{c}_{Hl,max}\boldsymbol{\sigma}_{Hl,ref}(\boldsymbol{x}) \tag{A.16}$$

For 2D plane stress state, $\partial \boldsymbol{\sigma}^j_{Hl,ref}/\partial \boldsymbol{\sigma}^j_{l,ref} = \left[\begin{array}{ccc} 1/3 & 1/3 & 0 \end{array}\right]^T$.

Based on the stress transformation equations in Eq. 8, the terms $\partial \boldsymbol{\tau}_{l,ref}(\theta)/\partial \boldsymbol{\sigma}_{l,ref}$ and $\partial \boldsymbol{\sigma}_{nl,ref}(\theta)/\partial \boldsymbol{\sigma}_{l,ref}$ are expressed as follows:

$$\begin{cases} \frac{\partial \boldsymbol{\tau}^j_{l,ref}(\theta)}{\partial \boldsymbol{\sigma}^j_{l,ref}} = \left[\begin{array}{ccc} -\frac{\sin 2\theta}{2} & \frac{\sin 2\theta}{2} & \cos 2\theta \end{array}\right] \\ \frac{\partial \boldsymbol{\sigma}^j_{nl,ref}(\theta)}{\partial \boldsymbol{\sigma}^j_{l,ref}} = \left[\begin{array}{ccc} \frac{1+\cos 2\theta}{2} & \frac{1-\cos 2\theta}{2} & \sin 2\theta \end{array}\right] \end{cases} \tag{A.17}$$

The derivative of the stress to the displacement can be deduced through Eq. 7:

$$\frac{\partial \boldsymbol{\sigma}_{l,ref}}{\partial \boldsymbol{u}_{l,ref}} = \boldsymbol{C}\overline{\boldsymbol{B}} \tag{A.18}$$

Finally, the following equation can be obtained:

$$\begin{aligned} \frac{\partial J^{(k)}}{\partial \rho_i} = \left(\boldsymbol{\mathcal{F}}^T\right)_i \Bigg\{ \frac{V_i}{|\Omega|} + \frac{1}{N}\Bigg[\left(\lambda_i^{(k)} + \mu^{(k)} h_i\right) p(1-\epsilon)\bar{\rho}_i^{(p-1)} g_i \left(g_i^2+1\right) \\ + p(1-\epsilon)\bar{\rho}_i^{(p-1)} \sum_{l=1}^{n_f} \left(\boldsymbol{\eta}_l^i\right)^T \boldsymbol{k}_0^i \boldsymbol{u}_{l.ref}^i \Bigg] \Bigg\} \frac{\beta\left\{1-\tanh\left[\beta\left(\tilde{\rho}_j-\eta\right)\right]\right\}^2}{\tanh(\beta\eta+\tanh[\beta(1-\eta)])} \end{aligned} \tag{A.19}$$

where $\boldsymbol{\mathcal{F}}_i$ is the i-th row of the filter matrix.

The Eq. A.19 under proportional loading can be simplified as follows:

$$\begin{aligned}\frac{\partial J^{(k)}}{\partial \rho_i} = \left(\boldsymbol{\mathcal{F}}^T\right)_i \Bigg\{ \frac{V_i}{|\Omega|} + \frac{1}{N} \Big[\left(\lambda_i^{(k)} + \mu^{(k)} h_i\right) p(1-\epsilon) \bar{\rho}_i^{(p-1)} g_i \left(g_i^2 + 1\right) \\ + p(1-\epsilon) \bar{\rho}_i^{(p-1)} \left(\boldsymbol{\eta}^i\right)^T \boldsymbol{k}_0^i \boldsymbol{u}_{ref}^i \Big] \Bigg\} \frac{\beta \left\{1 - \tanh\left[\beta\left(\tilde{\rho}_j - \eta\right)\right]\right\}^2}{\tanh(\beta\eta + \tanh[\beta(1-\eta)])}\end{aligned} \tag{A.20}$$

References

Braun, J., Sambridge, M., 1995. A numerical method for solving partial differential equations on highly irregular evolving grids. Nature 376, 655–660. doi:10.1038/376655a0.

Brighenti, R., Carpinteri, A., Vantadori, S., 2012. Fatigue life assessment under a complex multiaxial load history: An approach based on damage mechanics. Fatigue & Fracture of Engineering Materials & Structures 35, 141–153. doi:10.1111/j.1460-2695.2011.01600.x.

Bruggi, M., 2008. On an alternative approach to stress constraints relaxation in topology optimization. Structural and Multidisciplinary Optimization 36, 125–141. doi:10.1007/s00158-007-0203-6.

Chen, J.S., Wu, C.T., Yoon, S., You, Y., 2001. A stabilized conforming nodal integration for Galerkin mesh-free methods. International Journal for Numerical Methods in Engineering 50, 435–466. doi:10.1002/1097-0207(20010120)50:2<435::AID-NME32>3.0.CO;2-A.

Chen, Y., Monteiro, E., Imade, K., Favier, V., 2023. Stress constrained topology optimization using the constrained natural element method. Manuscript submitted for publication .

Chen, Z., Long, K., Wen, P., Nouman, S., 2020. Fatigue-resistance topology optimization of continuum structure by penalizing the cumulative fatigue damage. Advances in Engineering Software 150, 102924. doi:10.1016/j.advengsoft.2020.102924.

Chi, H., Talischi, C., Lopez-Pamies, O., Paulino, G.H., 2016. A paradigm for higher-order polygonal elements in finite elasticity using a gradient correction scheme. Computer Methods in Applied Mechanics and Engineering 306, 216–251. doi:10.1016/j.cma.2015.12.025.

Crossland, B., 1956. Effect of large hydrostatic pressures on the torsional fatigue strength of an alloy steel. International Conference on Fatigue of Metals: Proceedings, London, UK .

Dang Van, K., Griveau, B., Message, O., 1989. On a New Multiaxial Fatigue Limit Criterion: Theory and Application. Biaxial and Multiaxial Fatigue (EGF 3) , 479–496.

Dantas, R., Correia, J., Lesiuk, G., Rozumek, D., Zhu, S.P., de Jesus, A., Susmel, L., Berto, F., 2021. Evaluation of multiaxial high-cycle fatigue criteria under proportional loading for S355 steel. Engineering Failure Analysis 120, 105037. doi:10.1016/j.engfailanal.2020.105037.

Fatemi, A., Molaei, R., Sharifimehr, S., Shamsaei, N., Phan, N., 2017. Torsional fatigue behavior of wrought and additive manufactured Ti-6Al-4V by powder bed fusion including surface finish effect. International Journal of Fatigue 99, 187–201. doi:10.1016/j.ijfatigue.2017.03.002.

Findley, W.N., 1959. A Theory for the Effect of Mean Stress on Fatigue of Metals Under Combined Torsion and Axial Load or Bending. Journal of Engineering for Industry 81, 301–305. doi:10.1115/1.4008327.

Giraldo-Londoño, O., Paulino, G.H., 2021. Polystress: a matlab implementation for local stress-constrained topology optimization using the augmented Lagrangian method. Structural and Multidisciplinary Optimization 63, 2065–2097. doi:10.1007/s00158-020-02760-8.

Guest, J.K., Prévost, J.H., Belytschko, T., 2004. Achieving minimum length scale in topology optimization using nodal design variables and projection functions. International Journal for Numerical Methods in Engineering 61, 238–254. doi:10.1002/nme.1064.

Holmberg, E., Torstenfelt, B., Klarbring, A., 2014. Fatigue constrained topology optimization. Structural and Multidisciplinary Optimization 50, 207–219. doi:10.1007/s00158-014-1054-6.

Ibhadode, O., Zhang, Z., Sixt, J., Nsiempba, K.M., Orakwe, J., Martinez-Marchese, A., Ero, O., Shahabad, S.I., Bonakdar, A., Toyserkani, E., 2023. Topology optimization for metal additive manufacturing: current trends, challenges, and future outlook. Virtual and Physical Prototyping 18, e2181192. doi:10.1080/17452759.2023.2181192.

Jeong, S.H., Lee, J.W., Yoon, G.H., Choi, D.H., 2018. Topology optimization considering the fatigue constraint of variable amplitude load based on the equivalent static load approach. Applied Mathematical Modelling 56, 626–647. doi:10.1016/j.apm.2017.12.017.

Lindström, S.B., Thore, C.J., Suresh, S., Klarbring, A., 2020. Continuous-time, high-cycle fatigue model: Validity range and computational acceleration for cyclic stress. International Journal of Fatigue 136, 105582. doi:10.1016/j.ijfatigue.2020.105582.

Liu, J., Gaynor, A., Chen, S., Kang, Z., Suresh, K., Takezawa, A., Li, L., Kato, J., Tang, J., Wang, C., Cheng, L., Liang, X., To, A., 2018. Current and future trends in topology optimization for additive manufacturing. Structural and Multidisciplinary Optimization 57, 2457–2483. doi:10.1007/s00158-018-1994-3.

Liu, J., Zenner, H., 2003. Fatigue limit of ductile metals under multiaxial loading, in: Carpinteri, A., de Freitas, M., Spagnoli, A. (Eds.), European Structural Integrity Society. Elsevier. Biaxial/Multiaxial Fatigue and Fracture, pp. 147–164. doi:10.1016/S1566-1369(03)80009-2.

Matake, T., 1977. An Explanation on Fatigue Limit under Combined Stress. Bulletin of JSME 20, 257–263. doi:10.1299/jsme1958.20.257.

Matsubara, G., Hayashida, A., Kano, D., 2018. Predicting the multiaxial fatigue limit and the multiaxial high-cycle fatigue life based on the unified equivalent shear stress from axial strength characteristics with various waveforms. International Journal of Fatigue 112, 52–62. doi:10.1016/j.ijfatigue.2017.12.001.

Mower, T.M., Long, M.J., 2016. Mechanical behavior of additive manufactured, powder-bed laser-fused materials. Materials Science and Engineering: A 651, 198–213. doi:10.1016/j.msea.2015.10.068.

Nalli, F., Cortese, L., Concli, F., 2021. Ductile damage assessment of Ti6Al4V, 17-4PH and AlSi10Mg for additive manufacturing. Engineering Fracture Mechanics 241, 107395. doi:10.1016/j.engfracmech.2020.107395.

Oest, J., Lund, E., 2017. Topology optimization with finite-life fatigue constraints. Structural and Multidisciplinary Optimization 56, 1045–1059. doi:10.1007/s00158-017-1701-9.

Ottosen, N.S., Stenström, R., Ristinmaa, M., 2008. Continuum approach to high-cycle fatigue modeling. International Journal of Fatigue , 996–1006doi:10.1016/j.ijfatigue.2007.08.009.

Papadopoulos, I.V., 2001. Long life fatigue under multiaxial loading. International Journal of Fatigue , 839–849doi:10.1016/S0142-1123(01)00059-7.

Papadopoulos, I.V., Davoli, P., Gorla, C., Filippini, M., Bernasconi, A., 1997. A comparative study of multiaxial high-cycle fatigue criteria for metals. International Journal of Fatigue 19, 219–235. doi:10.1016/S0142-1123(96)00064-3.

París, J., Navarrina, F., Colominas, I., Casteleiro, M., 2009. Topology optimization of continuum structures with local and global stress constraints. Structural and Multidisciplinary Optimization 39, 419–437. doi:10.1007/s00158-008-0336-2.

Pejkowski, Ł., 2017. On the material's sensitivity to non-proportionality of fatigue loading. Archives of Civil and Mechanical Engineering 17, 711–727. doi:10.1016/j.acme.2016.09.010.

Rozvany, G.I.N., 1996. Difficulties in truss topology optimization with stress, local buckling and system stability constraints. Structural optimization 11, 213–217. doi:10.1007/BF01197036.

Sahadi, J.V., Paynter, R.J.H., Nowell, D., Pattison, S.J., Fox, N., 2017. Comparison of multiaxial fatigue parameters using biaxial tests of Waspaloy. International Journal of Fatigue 100, 477–488. doi:10.1016/j.ijfatigue.2017.01.019.

Senhora, F.V., Giraldo-Londoño, O., Menezes, I.F.M., Paulino, G.H., 2020. Topology optimization with local stress constraints: a stress aggregation-free approach. Structural and Multidisciplinary Optimization 62, 1639–1668. doi:10.1007/s00158-020-02573-9.

Sibson, R., 1981. A brief description of natural neighbor interpolation. Interpreting Multivariate Data , 21–36.

Sigmund, O., Petersson, J., 1998. Numerical instabilities in topology optimization: A survey on procedures dealing with checkerboards, mesh-dependencies and local minima. Structural optimization 16, 68–75. doi:10.1007/BF01214002.

Sines, G., 1959. Fatigue. McGraw Hill, New York , 145–169.

Skibicki, D., Pejkowski, Ł., 2019. The relationship between additional non-proportional hardening coefficient and fatigue life. International Journal of Fatigue 123, 66–78. doi:10.1016/j.ijfatigue.2019.02.011.

Slebioda, M., Giele, R., Langelaar, M., 2023. Topology optimization for infinite fatigue life of cyclic symmetric structures subjected to non-proportional loading. Computers & Structures 286, 107113. doi:10.1016/j.compstruc.2023.107113.

Socie, D., Marquis, G., 1999. Multiaxial Fatigue. SAE International.

Subedi, S., Verma, c.s., Suresh, K., 2020. A Review of Methods for the Geometric Post-Processing of Topology Optimized Models. Journal of Computing and Information Science in Engineering 20. doi:10.1115/1.4047429.

Sukumar, N., Moran, B., Belytschko, T., 1998. The natural element method in solid mechanics. International Journal for Numerical Methods in Engineering 43, 839–887. doi:10.1002/(SICI)1097-0207(19981115)43:5<839::AID-NME423>3.0.CO;2-R.

Suresh, S., Lindström, S.B., Thore, C.J., Torstenfelt, B., Klarbring, A., 2020. Topology optimization using a continuous-time high-cycle fatigue model. Structural and Multidisciplinary Optimization 61, 1011–1025. doi:10.1007/s00158-019-02400-w.

Talischi, C., Paulino, G., Pereira, A., Menezes, I., 2009. Polygonal finite elements for topology optimization: A unifying paradigm. International Journal for Numerical Methods in Engineering 82, 671–698. doi:10.1002/nme.2763.

Verbart, A., Langelaar, M., Keulen, F.v., 2016. Damage approach: A new method for topology optimization with local stress constraints. Structural and Multidisciplinary Optimization 53, 1081–1098. doi:10.1007/s00158-015-1318-9.

Verbart, A., Langelaar, M., Keulen, F.v., 2017. A unified aggregation and relaxation approach for stress-constrained topology optimization. Structural and Multidisciplinary Optimization 55, 663–679. doi:10.1007/s00158-016-1524-0.

Wang, F., Lazarov, B.S., Sigmund, O., 2011. On projection methods, convergence and robust formulations in topology optimization. Structural and Multidisciplinary Optimization 43, 767–784. doi:10.1007/s00158-010-0602-y.

Wang, Y.Y., Yao, W.X., 2004. Evaluation and comparison of several multiaxial fatigue criteria. International Journal of Fatigue 26, 17–25. doi:10.1016/S0142-1123(03)00110-5.

Wei, H., Liu, Y., 2020. An energy-based model to assess multiaxial fatigue damage under tension-torsion and tension-tension loadings. International Journal of Fatigue 141, 105858. doi:10.1016/j.ijfatigue.2020.105858.

Yvonnet, J., Ryckelynck, D., Lorong, P., Chinesta, F., 2004. A new extension of the natural element method for non-convex and discontinuous problems: the constrained natural element method (C-NEM). International Journal for Numerical Methods in Engineering 60, 1451–1474. doi:10.1002/nme.1016.

Zegard, T., Paulino, G.H., 2016. Bridging topology optimization and additive manufacturing. Structural and Multidisciplinary Optimization 53, 175–192. doi:10.1007/s00158-015-1274-4.

Zhang, S., Le, C., Gain, A., Norato, J., 2018. Fatigue-based topology optimization with non-proportional loads. Computer Methods in Applied Mechanics and Engineering 345, 805–825. doi:10.1016/j.cma.2018.11.015.